nature communications

Article

https://doi.org/10.1038/s41467-025-56100-9

Gout management using uricase and sodium citrate hollow mesoporous nanomotors

Received: 15 May 2024

Accepted: 9 January 2025

Lu Liu[1,2,5], Xiurong Li[2,5], Yongxian Chen[3,5], Junbin Gao[2], Yuejun Jiang[2], Yicheng Ye[2], Peng Wang[1], Fei Peng[4] & Yingfeng Tu[2]

Uricase (UOx)-based gout treatments are generally limited due in part to the accumulation of H_2O_2 in an arthrosis environment characterized by a sluggish metabolism. Here we develop a self-cascade nanomotor with high efficiency toward simultaneous uric acid (UA) degradation and H_2O_2 elimination on the basis of UOx and sodium citrate loading in amine functionalized hollow mesoporous silica nanoparticles (AHMSNs). Due to the inherent asymmetry of AHMSNs, the developed nanomotors can be actuated by ionic diffusiophoresis induced by the enzymatic UA degradation, thus enlarging the diffusion range within the joint cavity. H_2O_2 generated during UA decomposition can be simultaneously eliminated by the loaded sodium citrate, resulting in a considerable improvement in mammalian cell viability. In vivo studies display powerful therapeutic effect in gouty models using this self-cascade nanomotor system. These results present the potential of nanomotors as active therapeutic agents for gout, providing a perspective on the application of enzyme-driven micro/nanomotors.

Gout is the most common form of inflammatory arthritis caused by the accumulation of monosodium urate (MSU) crystals, a crystalline form of uric acid (UA), in and around the articular structures[1]. The current therapeutic approach for gout includes the transient alleviation of inflammation and discomfort during acute gout flares (corticosteroids, colchicine, and nonsteroidal anti-inflammatory drugs), as well as a prolonged therapy aiming to reduce the UA levels by lowering its reabsorption and suppressing its formation[2]. Nevertheless, these approaches result in severe adverse effects, such as urolithiasis, serve hypersensitivity reactions, and cardiovascular disease, which severely limit their clinical applications[3,4]. Uricase (UOx), being a highly effective oxidase, possesses the capability to catalyze the degradation of UA into allantoin[5], a compound with a higher solubility in water that contributes to the metabolism in the body. Therefore, UOx-based therapy would be an emerging and efficient approach for gout treatment[6]. Unfortunately, natural evolution has deprived the human species and several other advanced animals of the capability to express UOx[7]. Moreover, UOx still has some drawbacks: on the one hand, UOx exhibits numerous inherent deficiencies, including susceptibility to proteolytic digestion, easy damage in response to even minor alterations, etc[8]. on the other hand, a H_2O_2 byproduct is generated during UA degradation mediated by UOx[9]. In particular, slow metabolic in the joint cavity and the relatively enclosed interior environment exacerbate the buildup of H_2O_2 significantly, which results in oxidative stress as well as chronic joint injury. Thus, the development of an innovative system capable of self-protection and self-cleaning of the toxic intermediates is crucial for UOx-based gout therapies.

In the prior two decades, significant endeavors have been devoted to the development and fabrication of self-propelled micro/nanomotors[10–13]. Micro/nanomotors have demonstrated considerable potential in diverse fields, such as targeted drug delivery, mini-surgery, sensing and biomedicine, by virtue of their exceptional capabilities

---

[1]Pharmacy Department, The Fifth Affiliated Hospital of Southern Medical University, Southern Medical University, Guangzhou, China. [2]NMPA Key Laboratory for Research and Evaluation of Drug Metabolism & Guangdong Provincial Key Laboratory of New Drug Screening, School of Pharmaceutical Sciences, Southern Medical University, Guangzhou, China. [3]Medical Research Center, Sun Yat-Sen Memorial Hospital, Sun Yat-Sen University, Guangzhou, China. [4]School of Materials Science and Engineering, Sun Yat-Sen University, Guangzhou, China. [5]These authors contributed equally: Lu Liu, Xiurong Li, Yongxian Chen. e-mail: 13688860780@163.com; pengf26@mail.sysu.edu.cn; tuyingfeng1@smu.edu.cn

including efficient cargo transport, broad diffusion scope, and deep tissue penetration[14–17]. In contrast to passive nanoparticles, artificial micro/nanomotors possess the capability to execute autonomous motion through the conversion of powers from external stimuli or their own surroundings into mechanical forces[18,19]. The various driving forces of micro/nanomotors can be broadly divided into two types: external fields that are manually controlled (e.g., light, electric, ultrasonic, and magnetic)[20–23], and chemical fuels that exist within the system (e.g., water, hydrogen, urea, and H_2O_2)[24–26]. Enzyme-based micro/nanomotors are among the most prevalent chemical fuel powered motors, which rely on the highly efficient biocatalytic processes of intrinsic biofuels in natural biological hosts to produce a robust propelling force that surpasses random Brownian motion for effective autonomous motion[27,28]. Due to the exceptional specificity of reactions catalyzed by enzymes, enzyme-based micro/nanomotors exhibit a remarkable degree of preference towards biofuels[29,30]. Furthermore, due to the perpetual biofuel generation by the biological system, micro/nanomotors are capable of maintaining a consistent propulsive force for extended periods of self-propulsion. During the past decades, enzyme-based motors with different dimensions including 0D[31], 2D[32], and 3D[33–36] have been successfully developed. Even with significant progressions in the field of micro/nanomotors, only a few micro/nanomotors demonstrated autonomous motion in UA solution, and enzymatic motors capable of treating gout remain unexplored.

Here, we demonstrate an enzymatic hollow mesoporous nanomotor for efficient and friendly therapy for gout (Fig. 1). With a hole in the amine functionalized hollow mesoporous silica nanoparticles (AHMSNs), the as-prepared AHMSNs possess an intrinsic asymmetric property, different from the conventional method by depositing material onto a monolayer of particles to construct Janus structures. UOx and sodium citrate are then closely loaded onto AHMSNs to form a self-cascade catalytic system (AHMSNs@UOx@SC). AHMSNs@UOx@SC could be actuated by the UOx-triggered biocatalytic reaction of UA due to the asymmetric structure. The enhanced diffusion of UA-driven AHMSNs@UOx@SC could significantly expand its coverage area, resulting in more efficient gout therapeutic activity. This self-cascade catalytic system effectively degrades UA into allantoin and H_2O_2, while also catalyzing the conversion of the toxic byproduct H_2O_2 into oxygen (O_2) and H_2O with the assistance of the reductive effect of sodium citrate. In addition, the produced O_2 could further enhance the catalytic decomposition of UA, as the decomposition of UA involves the consuming of O_2. In vivo studies demonstrated that AHMSNs@UOx@SC could successfully treat gout in gouty models. Through a self-cascade catalytic reaction, serve joint swelling and inflammation induced by gout are effectively alleviated by AHMSNs@UOx@SC without any adverse effects. Besides, the equipped sodium citrate of our nanomotor could also raise the pH level of the local acidic microenvironment of synovial fluid, thereby increasing the solubility of UA and preventing UA stone formation. Such a self-

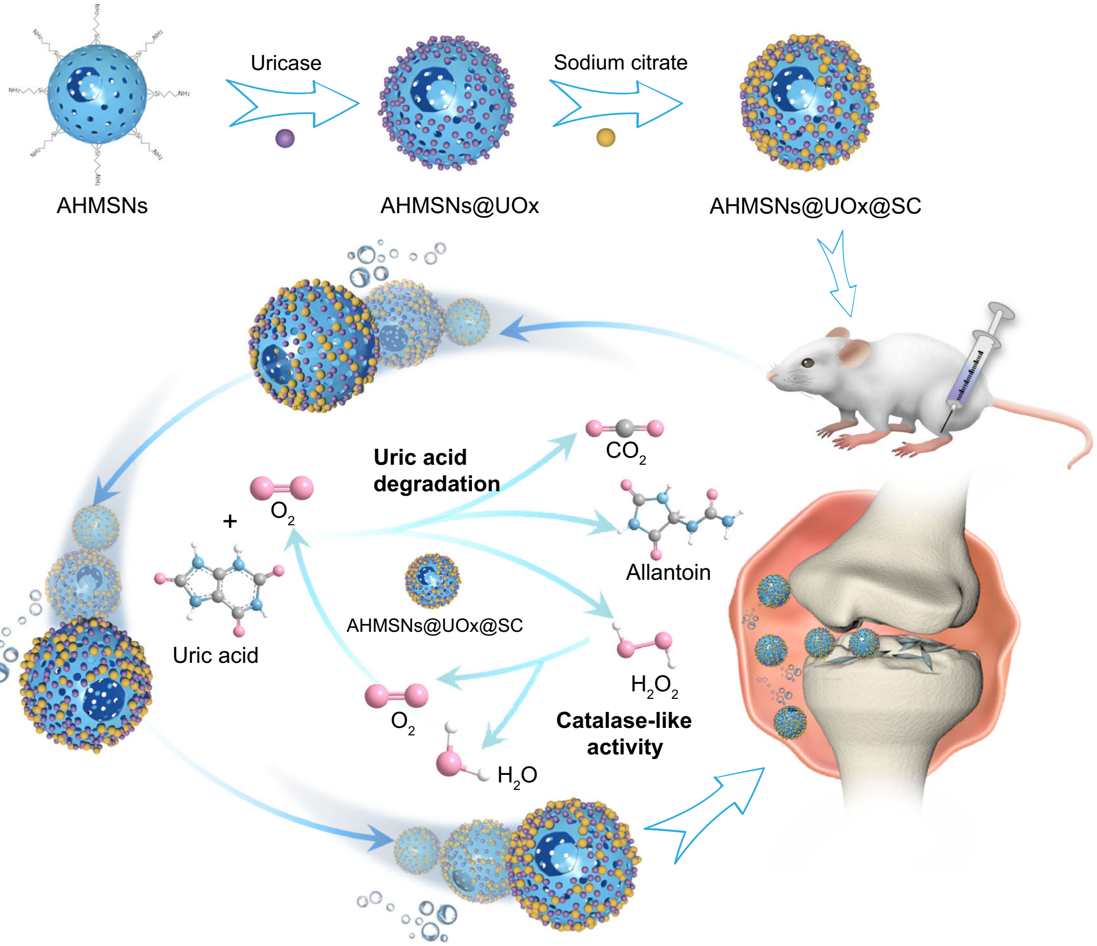

Fig. 1 | Schematic illustration of the design and fabrication of AHMSNs@UOx@SC nanomotor based on the self-cascade UA degradation for MSU-induced gout therapy. By closely loading UOx and sodium citrate onto AHMSNs, a self-cascade AHMSNs@UOx@SC is formed. When AHMSNs@UOx@SC nanomotors are administered in gouty joints, ionic diffusiophoresis induced by the UA degradation drives the enhanced diffusion of the motors. With active self-propulsion, the current system can extend its diffusion within the gouty joint cavity. Therefore, AHMSNs@UOx@SC is not only more effective in degrading UA but also exhibits exceptional H_2O_2 scavenging activities, which leads to a gout therapy that is both efficient and friendly.

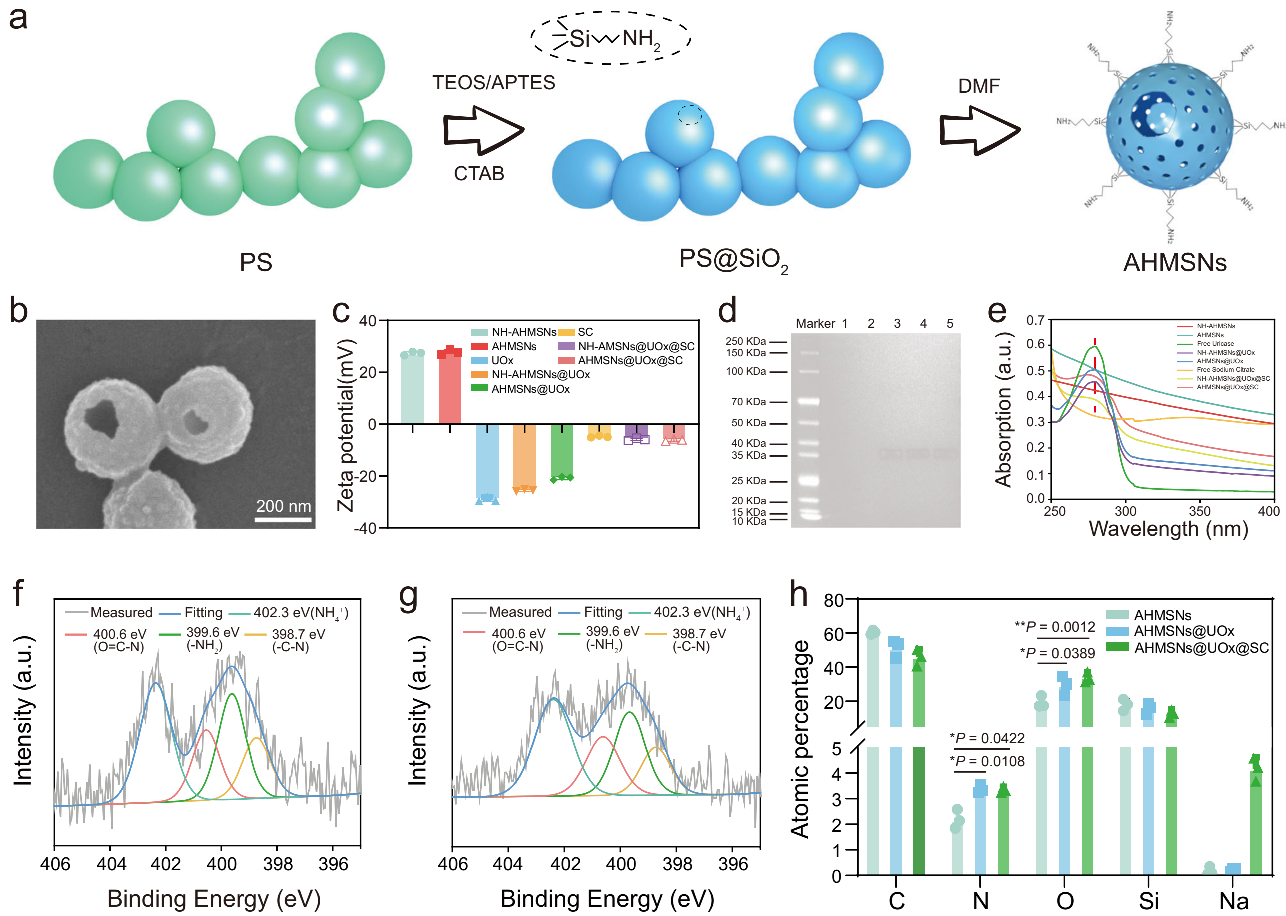

Fig. 2 | Fabrication and characterization of AHMSNs, AHMSNs@UOx, and AHMSNs@UOx@SC. a Schematic illustration of the formation of AHMSNs. Where the full name of PS is polystyrene, and the full name of DMF is dimethylformamide. **b** SEM image of AHMSNs. The experiment was repeated independently three times with similar results, and a representative result is shown. **c** Zeta potential of NH-AHMSNs, AHMSNs, UOx (Uricase), NH-AHMSNs@UOx, AHMSNs@UOx, SC (sodium citrate), NH-AHMSNs@UOx@SC, and AHMSNs@UOx@SC (*n* = 3 independent samples). **d** SDS-PAGE analysis of (1) NH-AHMSNs, (2) AHMSNs (3) UOx, (4) NH-AHMSNs@UOx, and (5) AHMSNs@UOx. The experiment was repeated independently three times with similar results, and a representative result is shown. **e** UV-vis absorption spectra of NH-AHMSNs, AHMSNs, free UOx, NH-AHMSNs@UOx, AHMSNs@UOx, free SC, NH-AHMSNs@UOx@SC, and AHMSNs@UOx@SC. High-resolution N1s spectra of AHMSNs (**f**) and AHMSNs@UOx (**g**). **h** *XPS* analysis of AHMSNs, AHMSNs@UOx, and AHMSNs@UOx@SC (*n* = 3 independent samples). In **c**–**h**, the full name of UOx is Uricase, the full name of SC is sodium citrate. Data in **c** and **h** are the mean ± S.D. *P* values were analyzed by Student's *t*-test (two-tailed). *$P < 0.05$ and **$P < 0.01$. Source data are provided as a Source Data file.

powered platform has the potential to offer valuable insights into the utilization of the enzyme-based nanomotors and possess considerable clinical translation potential in the management of gout.

Results

Fabrication and Characterization of AHMSNs@UOx@SC

As shown in Fig. 2a, AHMSNs functionalized with amine groups were synthesized by cocondensation method utilizing polystyrene (PS) nanoparticles as templates[37]. In Supplementary Fig. 1, the scanning electron microscope (SEM) images of PS nanoparticles with a diameter of 362.0 ± 5.9 nm are shown. Typically, the highly concentrated PS templates are packed closely together, allowing silica to only grow on the surfaces that are exposed. By removing the PS templates, we then characterized the morphology of as-prepared AHMSNs by SEM. A large hole with average diameters of 85.8 ± 21.3 nm was found on the hollow spheres, causing structural asymmetry for the nanomotors (Fig. 2b, Supplementary Fig. 2). The large hole was formed as a result of particle attachment during the "solgel" growth of the silica shell. Strong vortex treatment during the washing process caused the circular shell area that was interacting with other particles to be further pushed off by mechanical power. Additionally, the pore on the shell facilitated the dissolution and removal of the PS template by dimethylformamide. As shown in Supplementary Fig. 3a, AHMSNs demonstrated a typical Type IV isotherm curves with surface area of 839.3 m^2 g^{-1}. Based on the Barrett-Joyner-Halenda (BJH) desorption, the pore size distribution curve of AHMSNs indicated that the internal diameter was approximately 2.46 nm (Supplementary Fig. 4a). To compare the difference between AHMSN without holes (NH-AHMSNs) and AHMSNs, NH-AHMSNs was then prepared. As shown in Supplementary Fig. 5a, NH-AHMSNs showed a uniform hollow spherical structure. The size distribution acquired from Transmission electron microscopy (TEM) images showed that the size of NH-AHMSNs was 370.9 ± 17.6 nm in diameter (Supplementary Fig. 5b). NH-AHMSNs also showed type IV isotherm curves with surface area of 812.0 m^2/g (Supplementary Fig. 3b), similar to that of AHMSNs. NH-AHMSNs have a reduced mesopores internal diameter (approximately 2.43 nm) compared to AHMSNs (Supplementary Fig. 4b).

Afterward, glutaraldehyde (GA) was used as a linker to bind UOx to the external surface of NH-AHMSNs and AHMSNs, named as NH-AHMSNs@UOx and AHMSNs@UOx, respectively[38]. The zeta potential of NH-AHMSNs and AHMSNs dropped from positive (27.3 ± 0.5 mV and 27.7 ± 0.8 mV) to negative (−25.6 ± 0.3 mV and −20.8 ± 0.5 mV) after UOx modification, indicating that UOx had been successfully anchored (Fig. 2c). The encapsulation efficiency and the loading capacity of UOx in AHMSNs@UOx@SC was determined based on UV-Vis absorbance (Supplementary Fig. 6), which was approximately 75.08% and 35.62%, respectively. Furthermore, the sodium dodecyl sulfate-polyacrylamide gel electrophoresis (SDS-PAGE) result indicated that the protein profile of NH-AHMSNs@UOx and AHMSNs@UOx closely matched that of the pure UOx (Fig. 2d). UV-vis adsorption was then used to qualitatively characterize NH-AHMSNs@UOx and AHMSNs@UOx. As shown in Fig. 2e, the adsorption peak of NH-AHMSNs@UOx and AHMSNs@UOx at 279 nm (free UOx at 279 nm) demonstrated the successful cross-linking of UOx. X-ray photoelectron spectroscopy (*XPS*) studies additionally revealed the proof of UOx loading. The N1s *XPS* spectra in Fig. 2f, g and Supplementary Fig. 7 indicated that the N in NH_4^+, the N in O=C-NH group, the N in NH_2 group, and the N in C-N bond showed at 402.3 eV, 400.6 eV, 399.6 eV, and 398.7 eV respectively, as peaks of nitrogen-containing species[39]. Due to the high level of O=C-NH in UOx, the N and O element of AHMSNs@UOx and AHMSNs@UOx@SC was increased in comparison to AHMSNs, confirming the successful loading of UOx. Furthermore, the element content results (Fig. 2h) showed that compared with AHMSNs (2.19 ± 0.30 for N and 19.31 ± 2.83 for O), AHMSNs@UOx group achieved a significant increase in N and O element (3.37 ± 0.13 for N and 29.34 ± 4.68 for O, $P < 0.05$). Sodium citrate was then loaded onto NH-AHMSNs@UOx and AHMSNs@UOx through electrostatic interaction, named as NH-AHMSNs@UOx@SC and AHMSNs@UOx@SC. After introducing the negatively charged sodium citrate (−4.85 ± 0.29 mV), the zeta potential of NH-AHMSNs@UOx@SC and AHMSNs@UOx@SC increased from −25.57 ± 0.32 mV and −20.81 ± 0.50 mV to −5.89 ± 0.39 mV and -6.10 ± 0.36 mV, indicating the successful loading of sodium citrate. The atomic percentage of Na anchored on NH-AHMSNs@UOx@SC and AHMSNs@UOx@SC was 4.18% ± 0.20 and 4.17% ± 0.37% according to *XPS* analysis, compared with NH-AHMSNs and AHMSNs (0.17 ± 0.07% and 0.17 ± 0.13%), NH-AHMSNs@UOx and AHMSNs@UOx (0.22 ± 0.02% and 0.22 ± 0.06%), which is another evidence for the successful adsorption of sodium citrate (Fig. 2h and Supplementary Fig. 8).

Motion Analysis of AHMSNs@UOx@SC Nanomotors

The Janus structure has been intensively investigated as a prerequisite for micro/nanomotors, with the aim of producing directional self-propulsion via geometric asymmetry. In the present case, AHMSNs@UOx@SC utilizes the inherent asymmetry of the opening on the surface of the hollow structure, which is formed through a single-step chemical reaction. This asymmetry enables AHMSNs@UOx@SC to undergo phoretic motion, which is propelled by an enzymatic process involving the decomposition of UA by UOx to CO_2, H_2O_2 and allantoin. Figure 3a provides an illustration of the asymmetric structure of AHMSNs@UOx@SC and its motion, which is driven by UA decomposition. The phenomenon of self-propulsion in suitable substrate solutions by Janus nanoparticles that have been asymmetrically functionalized with enzymes is frequently elucidated through diffusiophoresis[40]. The symmetry of the hollow silica nanoparticles is inherently disrupted by the presence of holes; however, the mechanism by which the enzymatic process result in movement away from the opening remains unclear. To comprehend this mechanism of propulsion, we conducted numerical modeling of an AHMSNs@UOx@SC nanomotor whose outer surface is uniformly coated with UOx and sodium citrate, except for the area located at the hole. A model with 2D axisymmetry was built using the COMSOL Multiphysics package. As shown in Supplementary Fig. 9, the external dimeter of hollow silica sphere is 362 nm, and the internal dimeter is around 302 nm, and the dimeter of the hole is 86 nm. Carbonic acid (H_2CO_3) is formed when CO_2 (the products of AHMSNs@UOx@SC catalyzed UA) reacts with water; it subsequently divides into bicarbonate (HCO_3^-) and hydrogen ions (H^+). We presume a uniform outward flux of H^+ and HCO_3^- ions in this model. Due to the significantly rapid diffusion rate of H^+ in comparison to HCO_3^- (9.311×10^{-5} vs 1.185×10^{-5} cm^2 s^{-1}), an outwardly pointed electric field is generated spontaneously to preserve electroneutrality beyond the electrical double layers (in Fig. 3b). A hole on AHMSNs@UOx@SC surface causes a distortion in the electrical field and generates an electro-osmotic flow within the surface of the negative-charged particle, directing it towards the opening (Fig. 3c and Supplementary Fig. 10). Thus, an AHMSNs@UOx@SC nanomotor distances from its opening. In accordance with this simplified and qualitative model, we elucidated the motion properties of AHMSNs@UOx@SC motors moving via ionic diffusiophoresis. Figure 3d–h showed the typical UA-driven AHMSNs@UOx@SC tracking trajectories in the presence of 0, 200, 400, 600, and 1000 μM of UA, using optical video recording with a frame rate of 10 fps. The findings indicated that AHMSNs@UOx@SC without UA (namely 0 μM) only displayed Brownian motion. However, in the presence of UA, AHMSNs@UOx@SC demonstrated active self-propulsion with trajectories that increased in dependence on the concentration of UA. Supplementary movie 1 presents the typical video of AHMSNs@UOx@SC moving in varying concentration of UA solution. Mean-square-displacement (MSD) versus time interval (Δt) profiles for different UA concentrations were derived from the collected 2D coordinate (x, y) through the trajectories (Fig. 3i)[37]. The ascending slop values observed in the linear range of parabolic MSD curves in Fig. 3i until the UA concentration is up to 600 μM indicated a shift from Brownian diffusive motion to directed autonomous motion. To calculate the long-term translational diffusion coefficient (D_L), MSD was fitted to the equation ($D_L = MSD/4*\Delta t$) shown in Fig. 3j[41]. The D_L of AHMSNs@UOx@SC motors at 600 μM UA was significantly increased to a value of 1.9 ± 0.6 μm^2 s^{-1} when compared to Brownian motion without fuel. This result further supported that AHMSNs@UOx@SC nanomotors were indeed efficiently actuated by the asymmetric enzyme-catalytic chemical process. The velocity of the UA powered AHMSNs@UOx@SC in relation to the UA concentration was also calculated. Figure 3k showed that the velocity of the UA-driven AHMSNs@UOx@SC was increased as the UA concentration increased at the beginning, and it slightly decreased when the UA concentration further reached 1000 μM. It has been proposed that the enzymatic activity is rarely affected by low UA concentrations, and begins to saturate at a concentration of 600 μM. Subsequently, the enzymatic activity is suppressed by the inherent inhibition of UA at elevated concentrations, perhaps attributable to the reported denaturing impact of UA on proteins rivalry among UA and water[42].

We also investigated the motion behavior of AHMSNs@UOx motor at different concentrations of UA. Typical track trajectories of the UA powered AHMSNs@UOx at 0, 200, 400, 600, and 1000 μM UA are presented in Supplementary Fig. 11a–e. Similar to the movement property of AHMSNs@UOx@SC, the MSD curves in Supplementary Fig. 11f exhibit a linear range of increasing slope values until the UA concentration reaches 600 μM. However, the D_L of AHMSNs@UOx (1.35 ± 0.28 μm^2 s^{-1}) was significantly lower than AHMSNs@UOx@SC (1.91 ± 0.65 μm^2 s^{-1}, $P < 0.01$) under 600 μM UA (Supplementary Fig. 11g and Supplementary Fig. 12a). The velocity of the UA powered AHMSNs@UOx in relation to the UA concentration are shown in Supplementary Fig. 11h. Similarly, the velocity of AHMSNs@UOx under 600 μM UA was 5.26 ± 0.41 μm/s, which was significantly lower than that of AHMSNs@UOx@SC (7.19 ± 0.70 μm/s, $P < 0.0001$, Supplementary Fig. 12b). The findings of this study indicate that the degradation of H_2O_2 can be the extra driving force of AHMSNs@UOx @SC. This is due to the fact that sodium citrate initiates a cascade reaction that is catalyzed by UOx, which accelerates the catalytic degradation of UOx and as a result, accelerates the movement of AHMSNs@UOx@SC. Then, we studied the motion properties of NH-AHMSNs@UOx@SC in different concentrations of UA solutions. In contrast, the tracking trajectories and MSD profiles showed that NH-AHMSNs@UOx@SC exhibited a typical Brownian motion in different concentrations of UA solutions

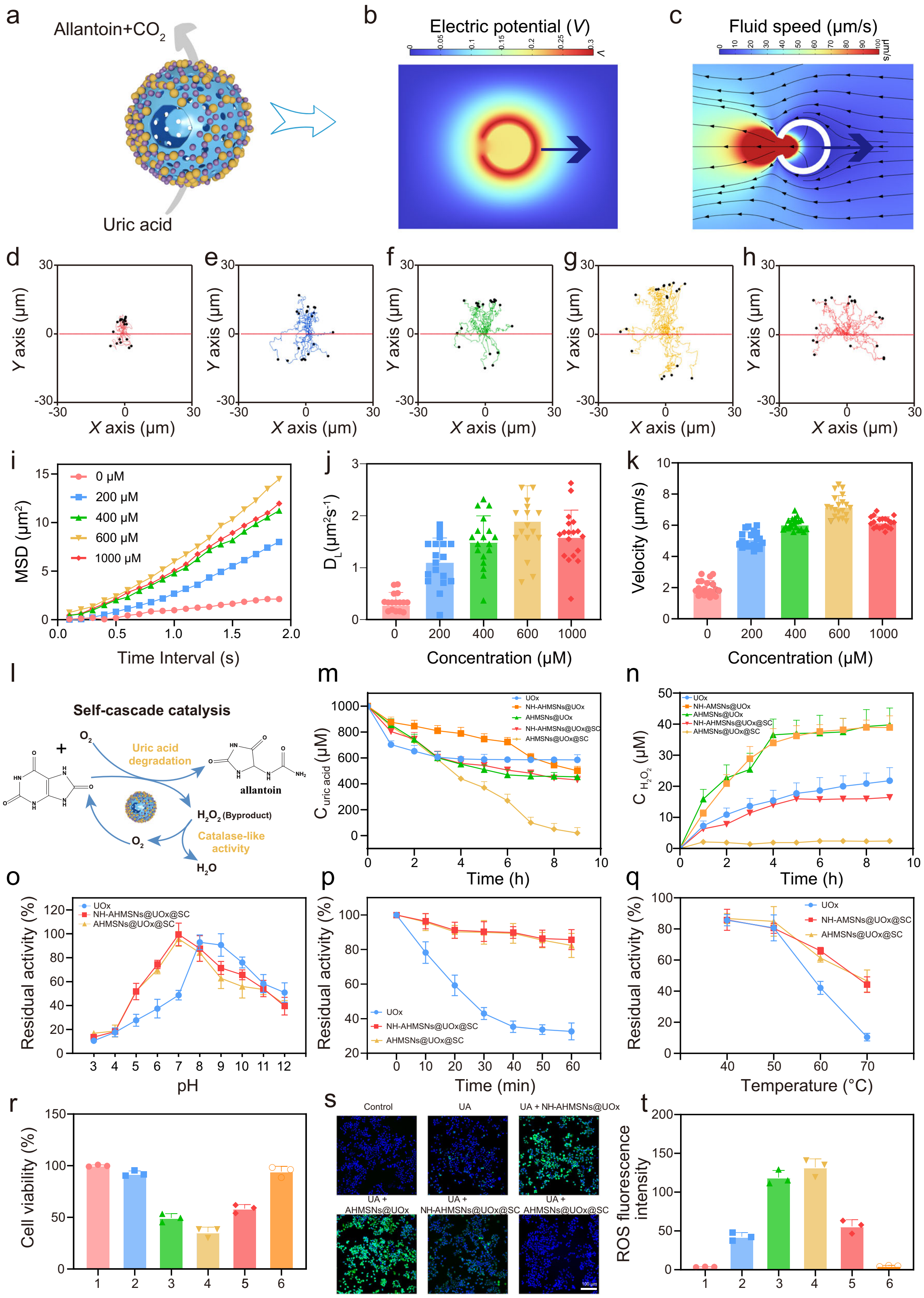

(Supplementary Fig. 13a–e). The almost stable D_L and the slowly increasing velocity, as shown in Supplementary Fig. 13f, g, also reflects the Brownian motion of NH-AHMSNs@UOx@SC. These data illustrated that AHMSNs@UOx@SC motors could be actuated efficiently in UA solution due to the asymmetric structure created by the hole structure compared to NH-AHMSNs@UOx@SC without holes, thereby supporting their potential for active gout therapy. Furthermore, we investigated the motion characteristics of enzymatically propelled AHMSNs@UOx@SC in saline (NaCl) solution and discovered that, at a UA concentration of 600 μM, the velocity of UA-driven AHMSNs@UOx@SC decreases as the NaCl concentration increases (Supplementary Fig. 14), which provides support for the ionic diffusiophoresis mechanism that we have postulated in our numerical model.

Fig. 3 | Performance characterization of AHMSNs@UOx@SC nanomotors. **a** Schematic illustration of AHMSNs@UOx@SC actuated by UA (Uric acid). **b** electrical potential distribution (color-code), and **c** flow field (black-arrow) of AHMSNs@UOx@SC driven by UA. Tracking trajectories of AHMSNs@UOx@SC nanomotors with varying concentrations of UA. (**d**) 0 μM, (**e**) 200 μM, (**f**) 400 μM, (**g**) 600 μM (**h**) 1000 μM. **i**, **j** MSD (Mean-square-displacement) and corresponding D_L (diffusion coefficient) with varied UA concentrations (*n* = 20 independent samples). **k** Velocity of AHMSNs@UOx@SC in UA solution with different UA concentrations (*n* = 20 independent samples). **l** Schematic illustration of the self-cascade catalysis by AHMSNs@UOx@SC. **m** UA degradation kinetics of AHMSNs@UOx@SC. The reaction was carried out in a 50 mM pH 8.0 phosphate buffer with 1000 μM UA and 250 μg/mL AHMSNs@UOx@SC at 25 °C (*n* = 3 independent samples). **n** H_2O_2 generation ability of AHMSNs@UOx@SC (*n* = 3 independent samples). UA degradation activity of AHMSNs@UOx@SC under various conditions, including different pH (**o**), trypsin (**p**), and high temperature (**q**) (*n* = 3 independent samples). **r** The viability of cells following a 12 h incubation under different conditions: (1) control; (2) UA; (3) UA with NH-AHMSNs@UOx; (4) UA with AHMSNs@UOx; (5) UA with NH-AHMSNs@UOx@SC; (6) UA with AHMSNs@UOx@SC. The starting concentration of UA was 1000 μM, and the UOx was fixed at 250 μg/mL (*n* = 3 independent samples). **s**, **t** Intracellular ROS (reactive oxygen species) detection via DCFH-DA (2′,7′-dichloroflurescein diacetate) and corresponding fluorescence intensity under different conditions (*n* = 3 independent samples). (1) control; (2) UA; (3) UA with NH-AHMSNs@UOx; (4) UA with AHMSNs@UOx; (5) UA with NH-AHMSNs@UOx@SC; (6) UA with AHMSNs@UOx@SC. The cells were stained with Hoechst (blue) and DCFH-DA (green). In **m**–**t**, the full name of UOx is uricase, and the full name of SC is sodium citrate. Data in **j**, **k**, **m**–**r**, and **t** are the mean ± S.D. Source data are provided as a Source Data file.

Enzymatic effects, H_2O_2 and ROS elimination ability of nanomotors

Following the successful fabrication of our enzymatic nanomotor, its capacity to catalytically degrade UA and the immediate toxicity of H_2O_2 were examined. Considering the UA levels of gout patients[43], a concentration of 1000×10^{-6} M UA was selected for the purpose of analyzing the degradation kinetics. The schematic of the self-cascade process triggered by AHMSNs@UOx@SC is depicted in Fig. 3l. The thorough degradation of UA within 9 h was shown in Fig. 3m, thereby confirming the notable efficacy of active AHMSNs@UOx@SC in UA degradation. In comparison, passive NH-AHMSNs@UOx@SC degraded only 57.0% of UA within 9 h. More intriguingly, during UA degradation, 16.4 ± 1.0 μM toxic H_2O_2 was produced from the passive NH-AHMSNs@UOx@SC, whereas negligible (2.4 ± 0.7 μM) toxic H_2O_2 production was observed for AHMSNs@UOx@SC, as shown in Fig. 3n. The observed differences in UA degradation and H_2O_2 elimination efficiency suggest that enhanced diffusion properties of AHMSNs@UOx@SC nanomotors in UA solutions. In addition, the system without sodium citrate (AHMSNs@UOx) accumulated toxic H_2O_2 (approximately reached 39.8 μM in 9 h) and had a lower rate of UA degradation. The increased rate of UA degradation in AHMSNs@UOx@SC compared with that in AHMSNs@UOx was attributed to the fact that the O_2 generated by sodium citrate facilitated the catalytic degradation of UA. Moreover, as a result of UOx denaturation, the activity of UOx in AHMSNs@UOx and UOx along systems decreased significantly after 3 h. These results showed the considerable benefits of our enzymatic nanomotor, which were explained by the attempts in two dimensions. First of all, the utilization of sodium citrate facilitated not only the catalytic elimination of the deleterious immediate H_2O_2, but also the acceleration of UA degradation via the produced O_2. Secondly, silica nanoparticles were used to further secure the UOx in the enzymatic nanomotor, thereby increasing its durability.

We then investigated the stability of AHMSNs@UOx@SC toward various challenges, including different pH, proteolytic digestion and high temperature. As depicted in Fig. 3o, the stability of free UOx in the pH = 8–10 range was attributed to its alkaline optimal pH[44]. NH-AHMSNs@UOx@SC and AHMSNs@UOx@SC was stable in the pH range of 6–11, which facilitated the active treatment in a weakly acidic gout microenvironment. Further investigation revealed that AHMNs@UOx@SC possessed a robust resistance to protease digestion. Free UOx retained only 32.6 ± 4.9% activity after being incubating with 1 mg/mL trypsin for 1 h, as illustrated in Fig. 3p. However, AHMSNs@UOx@SC could keep the activity of 82.4 ± 7.0% under the same conditions. The secondary structure change of UOx before and after the immobilization of AHMSNs in the presence of trypsin using circular dichroism (CD) spectroscopy were then investigated (Supplementary Fig. 15). As shown in Supplementary Fig. 15b, free UOx consists of 42.1% α-helix, 5.2% β-sheet, 21.5% β-turns, and 31.1% random coils. After incubation with trypsin for 1 h, the secondary secondary structure of free UOx changed significantly, as evidenced by a decrease in α-helix (30.9%) content and a simultaneous gradual increase in β-sheet (6.4%), β-turns (23.6%) and unordered structure (39.0%). However, the α-helix content of AHMSNs@UOx@SC exhibited only a slight reduction (41.9% to 37.9%) upon trypsin incubation, indicating no significant change in the secondary structure of the loaded UOx, which were consistent with the previously determined UOx activity. As shown in Fig. 3q, without silica layer, the activity of free UOx was nearly completely depleted after 30 min at 70 °C, while with the protection of silica layer, AHMSNs@UOx@SC and NH-AHMSNs@UOx@SC maintained 46.5 ± 7.1% and 44.2 ± 5.0% enzymatic activity under the same conditions respectively. Taken together, both of AHMSNs@UOx@SC and NH-AHMSNs@UOx@SC presented a significant protection effect under different pH, protease degradation, and high temperature. In addition, as shown in Supplementary Fig. 16, there was no change in the morphology of AHMSNs@UOx@SC and NH-AHMSNs@UOx@SC under PBS for three days. Supplementary Fig. 17 also demonstrated that the UOx activity of AHMSNs@UOx@SC did not decrease significantly under PBS during three days, indicating that AHMSNs@UOx@SC hold a capability of UA degradation in at least three days.

Then the cytotoxicity of the enzymatic nanomotor for gout therapy was examined and the results were illustrated in Fig. 3r. As anticipated, compared with NH-AHMSNs@UOx@SC (58.4 ± 3.3%), the cells in AHMSNs@UOx@SC group remained high viability (94.3 ± 4.2%). However, without sodium citrate, AHMSNs@UOx caused notable cytotoxic effects when degrading UA, resulting in a substantial fall in cell viability to 35.7 ± 4.0%. The higher cell viability in NH-AHMSNs@UOx (49.5% ± 3.3%) in comparison to AHMSNs@UOx (35.7% ± 4.0%) may be attributed to the enhanced diffusion of the asymmetric nanomotor, which leads to a more efficient degradation of UA, thereby generating more toxic H_2O_2. We speculated the production of poisonous H_2O_2, a common reactive oxygen species (ROS)[45], was primarily accountable for the cytotoxic effects. 2′,7′-dichloroflurescein diacetate (DCFH-DA), a nonfluorescent agent capable of reacting with intracellular ROS to produce DCF, was utilized to monitor ROS levels within the cells in order to validate the aforementioned hypothesis. Intracellular ROS concentration was correlated with the fluorescence intensity of DCF. Higher intracellular ROS fluorescence after NH-AHMSNs@UOx@SC treatment was observed when compared with that of AHMSNs@UOx@SC incubation, as illustrated in Fig. 3s, t. The quantitative analysis with flow cytometry further confirmed the similar results (Supplementary Fig. 18). In particular, ROS signal exhibited in NH-AHMSNs@UOx@SC was nearly 4.9 times greater than that of AHMSNs@UOx@SC (Supplementary Fig. 18b). These results highlighted the importance of enhanced diffusion of motors, which likely helped to increase the interaction of AHMSNs@UOx@SC nanomotors with UA, thus leading to enhanced gout therapy with minimal toxic adverse effects.

AHMSNs have typically been the topic of ongoing research discussions regarding their biocompatibility and degradability. The reason for this concern is that in order to avoid serious and unexpected

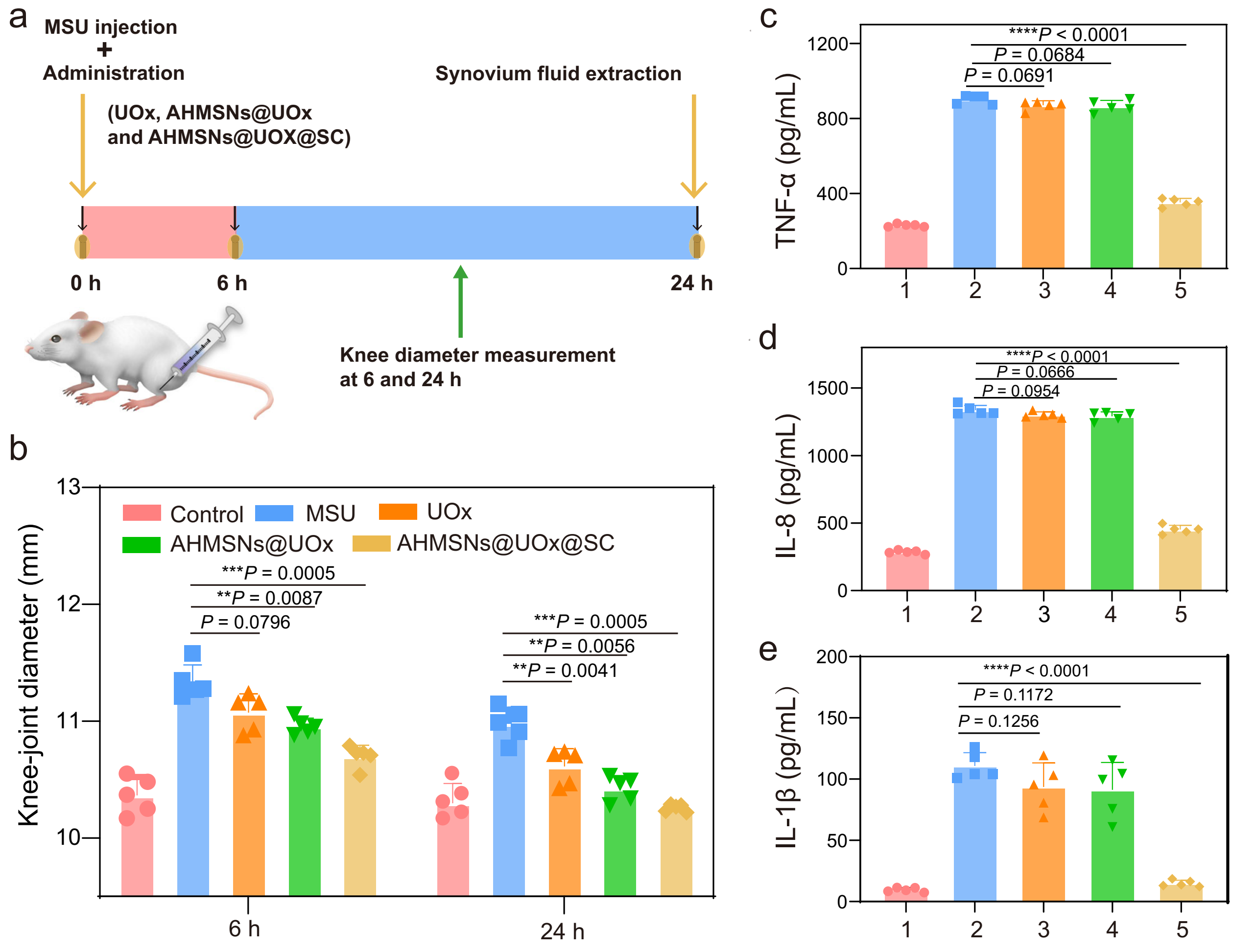

Fig. 4 | MSU(monosodium urate)-induced acute gouty model. a The experimental scheme of acute gout rat model. **b** The diameter of the right hind knee joint in 5 groups after 6 and 24 h following MSU crystal injection ($n = 5$ independent samples). For the data in Fig. 4b, $^{**}P < 0.01$, $^{***}P < 0.001$, the exact P value between MSU and UOx group at 6 h was 0.0796. **c**–**e** The inflammatory factors, including TNF-α, IL-8 and IL−1β, were extracted from synovial fluid of the right hind knee joints of rats (1: control; 2: MSU; 3: UOx; 4: AHMSNs@UOx; 5: AHMSNs@UOx@SC) ($n = 5$ independent samples). For the data in Fig. 4c, $^{****}P < 0.0001$, the exact P value between MSU and UOx group was 0.0691, and exact P value between MSU and AHMSNs@UOx was 0.0684. For the data in Fig. 4d, $^{****}P < 0.0001$, the exact P value between MSU and UOx group was 0.0954, and exact P value between MSU and AHMSNs@UOx was 0.0666. For the data in Fig. 4e, $^{****}P < 0.0001$, the exact P value between MSU and UOx group was 0.1256 and exact P value between MSU and AHMSNs@UOx was 0.1172. In (**a**–**e**), the full name of MSU is monosodium urate, the full name of UOx is uricase, and the full name of SC is sodium citrate. Data in b-e are the mean ± S.D. P values were analyzed by Student's t-test (two-tailed). Source data are provided as a Source Data file.

side effects, allowed drugs must not accumulate in the body of an individual. AHMSNs are characterized by a hydrolytic instability that dissolves gradually into soluble in water silicic acid, which is the predominant form at low concentrations[46]. We analyzed the degradation of AHMSNs@UOx@SC sample in simulated synovial fluid (SSF) by TEM, and the results were presented in Supplementary Fig. 19. Compared with the starting AHMSNs@UOx@SC in Supplementary Fig. 19a, the spherical shape and the pore structure were significantly altered after 5 days in SSF (Supplementary Fig. 19c). The residue exhibited a slightly smaller size and a rougher particle morphology. The sample was nearly completely dissolved after 9 days, and at this point, only few fragments were observed by TEM as displayed in Supplementary Fig. 19e, further confirming the degradability of AHMSNs@UOx@SC.

Therapeutic efficacy of AHMSNs@UOx@SC in Acute Gouty Arthritis Model

Having proving the viability of the enzymatic nanomotor in self-cascade reaction in vitro, we further conducted in vivo experiments. Monosodium urate(MSU) crystals were synthesized[44] and characterized by SEM images (Supplementary Fig. 20). Afterward, MSU were injected intra-articularly into the right knee joint of SD rats for the construction of an acute gout model. Then saline, UOx, AHMSNs@UOx, and AHMSNs@UOx@SC were injected separately into the joint intra-articularly in each group. The diameter of the right knee joint at 6 and 24 h was measured to evaluate the joint edema after treatments (Fig. 4a). The results of the study indicated that the swelling of the right knee joints in every group decreased to varying extents as time passed (Fig. 4b). There were not any statistically significant variations between MSU and UOx at 6 h following administration. However, statistically significant differences were observed between MSU and AHMSNs@UOx groups at all time points (post-administration) ($P < 0.01$). The observed results could potentially be attributed to the enhanced stability exhibited by UOx loading within AHMSNs and enhanced diffusion of AHMSNs@UOx motors. Encouragingly, AHMSNs@UOx@SC group had a significantly greater efficacy in alleviating acute gout flares compared to the MSU at time intervals of 6 and 24 h ($P < 0.001$). It was also demonstrated that the increased diffusion capability of AHMSNs@UOx@SC significantly relieves joint swelling caused by acute gout, as a consequence of the self-cascading reaction-induced acceleration of UA degradation.

In general, gout is consistently accompanied by an overabundance of immune cell recruitment, which results in the secretion of inflammatory factors[47]. Thus, ELISA kits were utilized to quantify inflammatory markers, such as TNF-α. IL-1β, and IL-8, that were extracted from the synovium fluid and the blood of the rats (Fig. 4c–e and Supplementary Fig. 21). Overall, the levels of nearly all three inflammatory cytokines decreased to different extents following treatments. AHMSNs@UOx@SC nanomotors noticeably suppressed the expression levels of the inflammatory cytokines compared with the MSU group (TNF-*α*, IL-8, and IL-1β, $P < 0.0001$). This is attributed to the fact that AHMSNs@UOx@SC could actively travel around within the joint cavity to approach much more MSU crystals compared to conventional passive nanoparticles, promising highly efficient gout efficacy. A similar trend was observed in H_2O_2 elimination levels within the rat joint cavity, as illustrated in Supplementary Fig. 22a. Contrary to expectations, unlike the alterations in joint diameter changes, the inflammatory cytokines and H_2O_2 content in AHMSNs@UOx@SC were still substantially higher compared to that in the control group. Therefore, the aforementioned findings indicate that the application of AHMSNs@UOx@SC treatment could solely alleviate the joint inflammation induced by MSU crystals, without achieving a complete cure. The observed differences between the variations in joint diameters, inflammatory cytokine and H_2O_2 levels indicate the necessity for further investigation.

Therapeutic efficacy of AHMSNs@UOx@SC nanomotors in recurrent gouty arthritis model

Acute gout is distinguished by its abrupt onset and the presence of severe discomfort in the joints of toes and other joints. Recurrent arthritic crises will result if effective therapy is not received. Consequently, the progression of recurrent gout episodes requires further clarification through the use of animal models. Here, the recurrent gouty arthritis model was then constructed[44]. Figure 5a provides a concise illustration of the experimental design. The right hind intraarticular knee of four groups of rats (excluding the control group) was injected with 100 μL of MSU crystals (20 mg/mL) under anesthesia on days 1 and 5, while the control group was simultaneously injected with 100 μL of PBS. For a period of seven weeks, the MSU and PBS injections were administered 14 times. Then UOx, AHMSNs@UOx and AHMSNs@UOx@SC were injected intra-articularly every four days from day 50 until the study endpoint (day 58). The joint swelling of each anaesthetized rats was captured and recorded after treatment. The macroscopic images depicting the right knee joints following repeated MSU injections are illustrated in Fig. 5b. The right knee of the MSU group exhibited substantial edema after seven weeks of repeated MSU injections. It was encouraging that the right knee joint swelling of the rats could be reduced to different extents by various treatments after the experiment concluded (24 h after the final intra-articular administration), including UOx, AHMSNs@UOx and AHMSNs@UOx@SC. The administration of UOx, AHMSNs@UOx, and AHMSNs@UOx@SC after MSU injection resulted in the diameter of the right knee joint being further relieved from 19.1 ± 0.4 mm of MSU group to 18.5 ± 0.4 mm, 13.5 ± 1.7 mm and 10.9 ± 1.0 mm, respectively (Fig. 5c). There was no discernible distinction between the MSU and UOx groups in terms of joint diameter. In contrast to the MSU group, the treatment of gout caused by MSU crystals was substantially alleviated by both AHMSNs@UOx and AHMSNs@UOx@SC. Obviously, compared with AHMSNs@UOx, it was evident that the AHMSNs@UOx@SC treatment was the superior option ($P < 0.0001$). The significant enhancement in the therapeutic efficacy of AHMSNs@UOx@SC for recurrent gout flares can likely be attributed to two primary factors. Firstly, UA-driven AHMSNs@UOx@SC can actively move and be exposed to more MSU crystals. Second, the self-cascading reaction occurring in AHMSNs@UOx@SC motors increases their active propulsion by accelerating the UA of degradation compared with AHMSNs@UOx and simultaneously eliminate the toxic H_2O_2 produced by UA, resulting in much higher possibility of relieving gouty joint swelling. The scavenging efficacy of AHMSN@UOx@SC on H_2O_2 within the joint cavity was examined, as shown in Supplementary Fig. 22b. The MSU group exhibited a significantly higher H_2O_2 level in the joint cavity (14.45 ± 0.27 mmol/gprot) than the control group (7.63 ± 0.23 mmol/gprot). Although the H_2O_2 level was evidently reduced in the presence of UOx (13.59 ± 0.56 mmol/gprot) and AHMSNs@UOx (13.11 ± 0.34 mmol/gprot) groups, the rat treated with AHMSNs@UOx@SC showed the lowest level (8.14 ± 0.41 mmol/gprot), which did not exhibit any discernible distinction from that of the control group (7.63 ± 0.23 mmol/gprot). In addition, it had been previously observed that the H_2O_2 generated by UA could be at the same time eliminated by AHMSNs@UOx@SC while AHMSNs@UOx systems exhibited substantial accumulation of hazardous H_2O_2. These results indicated that AHMSNs@UOx@SC exhibited a significant H_2O_2 scavenging effect in gout rat, which is attributable by not only the ability to enhance the diffusion via a self-cascade reaction, surpassing AHMSNs@UOx in achieving superior H_2O_2 scavenging efficacy, but also the incorporated sodium citrate, alighing with the results from in vitro cytotoxicity experiments.

The pH range of normal synovial fluid is typically observed to be between 7.4 and 7.8[48]. Within this specific pH range, the predominant form of UA is free urate. The conversion of UA from its free state to urate in the bound state occurs gradually as the pH falls. Subsequently, urate precipitates as crystals, resulting in the occurrence of gouty flares. Here, the pH of the synovial fluid within the joint cavity of the rats with recurrent gout was measured. As presented in Fig. 5d, the pH of the synovial fluid in MSU group was significantly less that of the control group, but virtually identical to that of UOx group. Despite the fact that the pH level of the AHMSNs@UOx groups was evidently increased, the rat treated with AHMSNs@UOx@SC motor showed the highest pH level. The reason for this result may be the active AHMSNs@UOx@SC motors can “on the fly” gain more exposure to MSU crystals by enhanced diffusion via self-cascade reaction compared with AHMSNs@UOx. Moreover, the ability of the sodium citrate loaded on AHMSNs@UOx@SC motor to alkalizes the synovial fluid and eliminate the weakly acidic H_2O_2 in the joint cavity result the much higher possibility of maintaining the acid-base balance in the gout microenvironment.

Furthermore, the weight changes during the administration were found to be normal in each group of the rats in a recurrent gouty arthritis model (Fig. 5e), further indicating that the our artificial enzymatic nanomotor exhibited favorable biological safety. In terms of the changes in the degree of joint swelling and H_2O_2 scavenging, a similar trend of plasma inflammatory factor levels was also observed. As shown in Fig. 5f-h, inflammatory factors in plasma such as TNF-α, IL-8, and IL-1β were increased after inducing recurrent gout flares. AHMSNs@UOx and AHMSNs@UOx@SC treatment suppressed the inflammatory cytokines (TNF-α, IL-8, and IL-1β) but individual UOx injection did not, indicating that the therapeutic effect of AHMSNs@UOx and AHMSNs@UOx@SC motors in gout may result from the superiority of enhanced diffusion and the protection of UOx. Compared with the AHMSNs@UOx group, AHMSNs@UOx@SC motors accompanied with faster diffusion due to self-cascading reactions additionally down-regulated the expression levels of TNF-α, IL-8, and IL-1β to a more remarkable level and were significantly distinct from the control group. Taken together, the results indicated that our AHMSNs@UOx@SC nanomotor possessed prominent anti-inflammatory effects in recurrent gouty rat.

The reconstructed three-dimensional illustrations of the typical micro-CT images of five groups are displayed in Fig. 5i. Anterior-posterior perspectives and trabecular of the knee joint illustrate the changes in bone microstructure and morphology. In comparison to the control group, the MSU group exhibited a decrease in trabecular

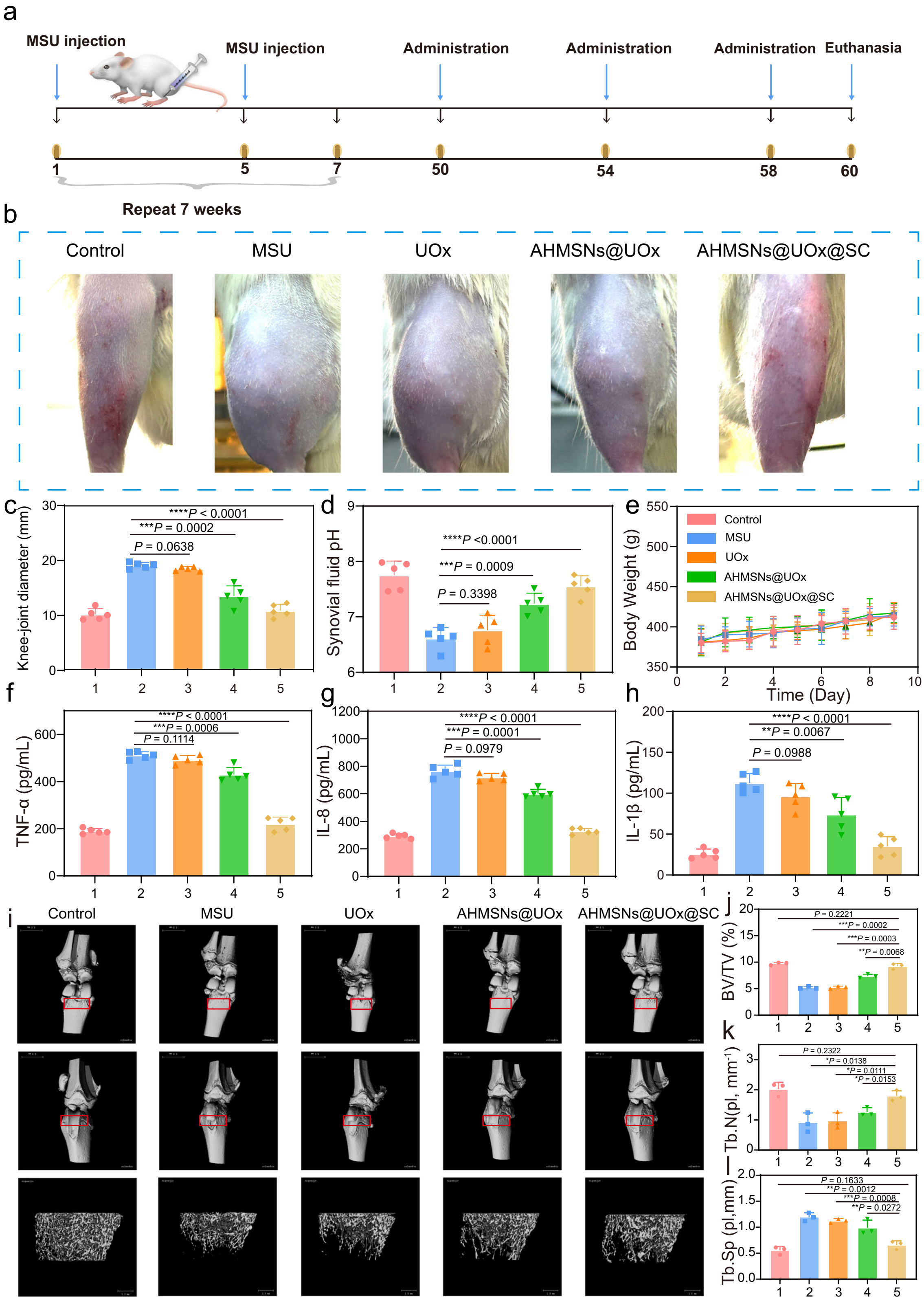

growth traces from the top to the bottom. However, under various treatment conditions, trabecular growth was alleviated to varying degrees, with the AHMSNs@UOX@SC group experiencing the greatest reduction. Further morphometric analysis was conducted on CT images in order to compare the indicators associated with bone structure within each group. The calculation of BV/TV was performed in Fig. 5j to represent the bone bulk of subchondral trabecular bone. For AHMSNs@UOx@SC group (9.2 ± 0.4), the BV/TV was much higher than that of the MSU group (5.2 ± 0.2, $P < 0.001$), with minimal distinction from the control group (9.7 ± 0.2). As a result, the bone mass loss induced by MSU crystals may be significantly reduced by AHMSNs@UOx@SC. Tb.N and Tb.Sp are primarily associated with the spatial structure of subchondral trabecular bone; In general, an increase in Tb.N value corresponds to a lower Tb.Sp value, indicating a

Fig. 5 | MSU-induced recurrent gouty model. a The experimental design for the establishment of MSU-induced recurrent gouty model and active treatments. **b** Macroscopic images of the right knee joints from the groups of control, MSU, UOx, AHMSNs@UOx and AHMSNs@UOx@SC. **c**, **d** Knee-joint diameter and synovial fluid pH of the affected limbs of the rats at 24 h after the last intra-articular administration ($n = 5$ independent samples). (1: control; 2: MSU; 3: UOx; 4: AHMSNs@UOx; 5: AHMSNs@UOx@SC). For the data in Fig. 5c, ****$P < 0.0001$, ***$P < 0.001$, and the exact P value between MSU and UOx group was 0.0638. For the data in Fig. 5d, ****$P < 0.0001$, ***$P < 0.001$, and the exact P value between MSU and UOx group was 0.3398. **e** Weight changes of the rats during the administration process ($n = 5$ independent samples). (1: control; 2: MSU; 3: UOx; 4: AHMSNs@UOx; 5: AHMSNs@UOx@SC). **f**–**h** Inflammatory factors of the blood collected by the cardiac punctures of the rats from the five groups, including TNF-α, IL-8, and IL−1β (n = 5 independent samples). (1: control; 2: MSU; 3: UOx; 4: AHMSNs@UOx; 5: AHMSNs@UOx@SC). For the data in Fig. 5f, ****$P < 0.0001$, ***$P < 0.001$, and the exact P value between MSU and UOx group was 0.1114. For the data in Fig. 5g, ****$P < 0.0001$, ***$P < 0.001$, and the exact P value between MSU and UOx group was 0.0979. For the data in Fig. 5h, ****$P < 0.0001$, **$P < 0.01$, and the exact P value between MSU and UOx was 0.0988. **i** Representative three-dimensional CT reconstruction images of the right hind knee joints of the rats. **j**–**l** The indicators pertaining to the bone structure of the right knee joints of rats in each group are as follows: BV/TV, Tb.N, and Tb.Sp ($n = 3$ independent samples). For the data in Fig. 5j, ***$P < 0.001$, **$P < 0.01$, and the exact P value between control and AHMSNs@UOx@SC group was 0.2221. For the data in Fig. 5k, *$P < 0.05$, and the exact P value between control and AHMSNs@UOx@SC group was 0.2322. For the data in Fig. 5l, **$P < 0.01$, ***$P < 0.001$, and the exact P value between control and AHMSNs@UOx@SC group was 0.1633. In **a**–**l**, the full name of MSU is monosodium urate, the full name of UOx is uricase, and the full name of SC is sodium citrate. Data in **c**–**h** and **j**–**l** are the mean ± S.D. P values were analyzed by Student's t-test (two-tailed). Source data are provided as a Source Data file.

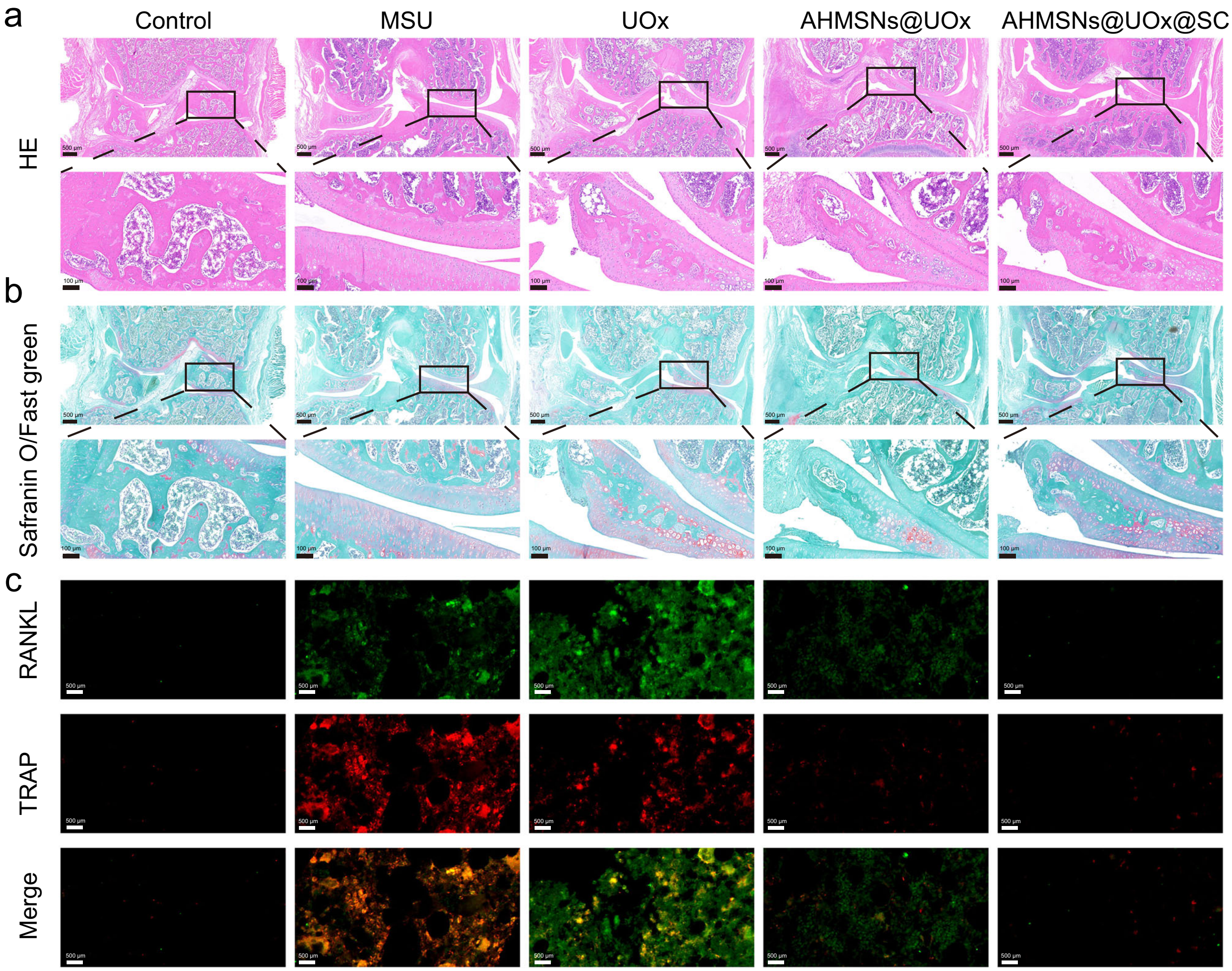

Fig. 6 | Histopathological analysis of the histopathology of MSU-induced recurrent gouty model after different treatments. Representative H&E (**a**), Safranin O/Fast green (**b**), and double-immunofluorescent (**c**) staining on the RANKL (green) and TRAP (red) images for knee joints of the control, MSU, UOx, AHMSNs@UOx, and AHMSNs@UOx@SC group. The full name of MSU is monosodium urate, the full name of UOx is uricase, and the full name of SC is sodium citrate. In **a**–**c**, the experiments were repeated independently three times with similar results, and a representative result is shown for each. Source data are provided as a Source Data file.

greater propensity for anabolism rather than catabolism of bone[49]. The results of the plate model for Tb.Sp and Tb.N were illustrated in Fig. 5k-l. The plate model results indicated that in contrast to the MSU group (1.2 ± 0.1 mm for Tb.Sp and $0.9 \pm 0.3\,\text{mm}^{-1}$ for Tb.N), AHMSNs@UOx@SC achieved a significant decrease in bone trabecular separation and an increase in trabecular number (0.7 ± 0.1 mm for Tb.Sp, $P < 0.01$, and $1.8 \pm 0.1\,\text{mm}^{-1}$ for Tb.N, $P < 0.1$), and had a similar level to that of the control rats (0.6 ± 0.1 mm for Tb.Sp and $2.0 \pm 0.2\,\text{mm}^{-1}$ for Tb.N). These results demonstrated that active motion of our AHMSNs@UOx@SC motors and accelerated UA degradation due to self-cascade reaction had tremendous superiority in preventing bone catabolism caused by MSU crystal injury.

For in vivo elimination of AHMSNs@UOx@SC, in vivo imaging was employed to evaluate the elimination dynamics of the nanomotors within the joint cavity of the rats with recurrent gouty arthritis (Supplementary Fig. 23a). The results indicated that the fluorescence intensity of Cy7-labeled AHMSNs@UOx@SC nanomotors reached its peak immediately before gradually diminishing. Nearly no fluorescence was observed after 72 h (Supplementary Fig. 23b). This in vivo result differs slightly from the previously mentioned degrading behavior of motors in SSF, as the concentration employed for injecting Cy7-labled AHMSNs@UOx@SC into joint is far below saturation level (145 μg/mL)[50]. Furthermore, nanomotors in the joint encounter a flowing medium that eliminates dissolution products, hence minimizing re-precipitation and aggregation. Therefore, the in vivo elimination behavior occurs on an hour-scale and may be impeded with respect to synovial fluid in the joint cavity due to the adsorption of proteins and other biomolecules onto the nanomotor surface[51]. The elimination kinetics of AHMSNs@UOx@SC in gouty rats were also analyzed using microdialysis (Supplementary Fig. 23c, d and Supplementary Fig. 24). The results indicated that the nanomotors were gradually eliminated from the joints and the circulation. At 72 h, silicon concentrations were nearly negligible in both joint and circulation, which was consistent with the in vivo imaging results. The results demonstrate that AHMSNs@UOx@SC exhibit rapid and hour-scale elimination kinetics in vivo, exhibiting its excellent biocompatibility.

Histopathological Evaluation of Nanomotor In Vivo

Furthermore, the histopathological analysis, including H&E, safranin O/fast green, and TRAP staining, of the right knee joint of the rats was conducted to assess the therapeutic effectiveness of our active AHMSNs@UOx@SC. The MSU group exhibited a severe inflammatory response, as demonstrated by the massive infiltration of immune cells and synovial villous hyperplasia in the H&E-stained images of the synovial tissue (Fig. 6a). AHMSNs@UOx@SC group exhibited a notable decrease in immune cells and synovial villous hyperplasia, suggesting that its potent anti-inflammatory effect surpassed that of the UOx and AHMSNs@UOx group, comparable to those of the control group. Significant joint edema was observed in the Safranin O/fast green staining images of the MSU group, which were diminished by UOx, AHMSNs@UOx, and AHMSNs@UOx@SC group (see Fig. 6b). For comparative quantification of histopathological evaluation, the total cartilage degeneration width (T_{cdw}) and significant cartilage degeneration width (S_{cdw}) were extracted from these images. AHMSNs@UOx@SC motors showed the best therapeutic effect in both T_{cdw} (4.09 ± 0.22 mm for the MSU group and 2.36 ± 0.07 mm for AHMSNs@UOx@SC group, $P < 0.001$) and S_{cdw} (2.07 ± 0.06 mm for MSU group and 0.19 ± 0.07 mm for AHMSNs@UOx@SC group, $P < 0.0001$) than UOx (2.95 ± 0.08 mm for T_{cdw}, $P < 0.01$) and AHMSNs@UOx (1.08 ± 0.09 mm for S_{cdw}, $P < 0.001$), as the data listed in Supplementary Fig. 25. Then, the involvement of the RANK/RANKL pathway in the joint destruction of the recurrent gouty arthritis model induced by MSU was confirmed (Fig. 6c). A significant degree of overlap was observed between RANKL-positive and Tartrate Resistant Acid Phosphatase (TRAP)-positive cells in the MSU group, whereas the control group did not contain any cells expressing either RANKL or TRAP. It was suggested that the formation of osteoclasts induced by MSU occurred via osteoclast maturation induced by RANKL. The amount of TRAP- and RANKL-positive cells would be reduced by the treatment of UOx or AHMSNs@UOx. However, fewer RANKL- and TRAP-positive cells were observed in the AHMSNs@UOx@SC group. The findings of the study suggest that the potent effect of AHMSNs@UOx@SC motors for recurrent gouty therapy was caused by the enhanced diffusion through consuming the MSU crystals in the joints, as well as accelerating the degradation of UA and elimination of toxic H_2O_2 via a self-cascade reaction.

Discussion

In summary, we have developed an effective and safe approach for the active treatment of gout based on artificial enzymatic nanomotors. Instead of forming Janus structures, AHMSNs@UOx@SC with intrinsic asymmetry generated by a one-step chemical process could execute active motion powered by biocompatible fuel of UA, allowing for future mass manufacturing by bulk solution synthesis. This system exhibited both durable and excellent catalytic activity to UA degradation but also simultaneously eliminated the produced hazardous intermediate H_2O_2 by sodium citrate in vitro. Meanwhile, the as-prepared AHMSNs@UOx@SC are highly self-protective against various challenges, such as different pH, proteases, and high temperature. Furthermore, AHMSNs@UOx@SC nanomotors could be degraded when exposed to SSF, indicating their excellent biocompatibility. In vivo studies displayed prominent therapeutic efficacy and no apparent side effects during the treatment of gout rat using our designed artificial enzymatic nanomotor. Furthermore, the enzyme nanomotor could raise the pH level of synovial fluid in the rats with gout, which in turn maintains the acid-base balance of the synovial fluid. Consequently, AHMSNs@UOx@SC exhibited an effective therapeutic effect in the management of gout, indicating the potential of AHMSNs@UOx@SC as a therapeutic agent for the effective treatment of gout. Overall, such a platform not only facilitates the development of the functionalization of micro/nanomotors, but also offers perspectives of enzymatic micro/nanomotors for biomedical applications.

Methods

Cell Lines and Animals

RPMI-1640 complete medium (Procell, CM-0007) was used to cultivate 4T1 (Mouse mammary tumor) cells (Lot: XRBETC2TZM) that were purchased from Procell Life Science&Technology Co., Ltd. The cells were incubated at 37 °C in a humidified incubator with 5% CO_2. The Laboratory Animal Center of Southern Medical University provided male SD rat (5–6 weeks old, 180–220 g). The rats were permitted to consume food and water at their discretion, and they were maintained in an ambient temperature range of 22–24 °C, with a humidity level of 30-70%, and a 12-hour light/dark cycle. All the animal procedures were carried out under the guidelines approved by the Institutional Animal Care and Use Committee (IACUC) of the Southern Medical University (Permit number: SMUL202403035).

Materials

Polyvinylpyrrolidone (K-30, >98%), ethanol (EtOH, >99%), dimethylformamide (DMF, >99%), glutaraldehyde (GA, 25% in H_2O), and uric acid (UA) were obtained from Aladdin. Isopropanol (IPA), Styrene, 2,2′-azo-bis(isobutyronitrile) (AIBN, 98%), Ammonia ($NH_3 \cdot H_2O$, 25%), 3-aminopropyltriethoxysilane (APTES, 99%), and MeOH were provided by Inno-Chem. Cetyltrimethylammonoium bromide (CTAB, 99%) was purchased from Sigma. Tetraethylorthosilicate (TEOS, 99%) was procured from Sigma-Aldrich. HCl was provide by Guangzhou Chemical Reagent Factory. UOx and Cy7-NHS were obtained by Macklin. Phosphate-buffered saline (PBS, pH = 6.5) buffer, Normal saline, and 4% paraformaldehyde were purchased by Biosharp. Sodium citrate was obtained by Shanghai Yuanye Bio-Technology Co., Ltd. Hydrogen peroxide assay kit, ROS Assay Kit, BCA protein assay kit, and Hoechst 33342 were purchased by Beyotime. NaOH was provided by Damao Chemical Reagent Factory. Rat TNF-α ELISA Kit, and Rat IL-8 ELISA kit were procured from Dakewe. HS Rat IL-1β (Interleukin 1 Beta) ELISA Kit was purchased by Elabscience.

Instruments

JEOL JEM-2100 F Transmission Electron Microscope (TEM) with an acceleration voltage of 120 kV was used for the characterization of nanomotor structure. The Zeiss Sigma 300 scanning electron microscope was employed to capture scanning electron microscope (SEM) images. The Malvern Zetasizer Nano ZSE was used to perform zeta potential measurements with the following parameters: He-Ne laser wavelength of 633 nm, temperature of 25 °C The UV-vis absorption was measured with a UV-2600 spectrophotometer (SHIMADZU, Japan). The ESCALAB 250XI X-ray photoelectron spectrometer was employed to conduct *XPS* analysis with Al/Mg as the exciting source. N_2 adsorption-desorption isotherms were obtained on Micromeritics ASAP 2460 automated sorption analyzer. Inductively Coupled Plasma Mass Spectrometry (ICP-MS) analyzes was performed on ICPOES 730 (Agilent). Cell morphology was captured with Nikon Ti2-A Inversion Fluorescence Microscope. Flow cytometry data were obtained via BD LSRFortessa X-20. In vivo imaging of rat was performed by AniView Kirin.

Preparation of PS Nanoparticles

A typical PS preparation with some modifications is shown below[48]. Initially, a mixture of 20 mL of deionized water and 180 mL of IPA was used to dissolve 1 g of K-30. Following the addition of styrene (40 g) and AIBN (0.68 g), The mixture was elevated to 70 °C. and stirred continuously for 24 h while subjected to nitrogen gas flux. A 1:1 mixture of ethanol and DI water was used to rinse the PS particles five times. The particles were then suspended in ethanol for future use.

Preparation of AHMSNs and NH-AHMSNs

PS (3.5 g), CTAB (1 g), and $NH_3{\cdot}H_2O$ (5 mL) were added into a solution consisting of 130 mL of deionized water and 100 mL of ethanol, which was subjected to sonication for 10 min. Then, 1.75 mL of TEOS was added into the mixture while stirring continuously. Following a reaction of 6 h, 300 µL of APTES was added. The mixture was stirred for an additional 16 h. The PS coated with mesoporous silica particles was collected and rinsed with ethanol three times. Subsequently, the PS template was removed by undergoing five washes with DMF, resulting in the formation of AHMSNs. CTAB was eliminated by suspending the acquired AHMSNs in 10 mL of MeOH containing 37% HCl (600 µL). The solution was then shaken at room temperature for 2 h before centrifugation (4660 g) to collect the particles. Following three washes with a solution of ethanol and DI water, AHMSNs were subsequently dispersed in DI water for future use.

Preparation of AHMSNs@UOx and NH-AHMSNs@UOx

UOx-conjugated AHMSNs and NH-AHMSNs, denoted as AHMSNs@UOx and NH-AHMSNs@UOx, were synthesized by employing GA as a linker molecule. In general, AHMSNs and NH-AHMSNs acquired in the previous step were suspended in a solution of PBS buffer (pH = 6.5) supplemented with GA (2.5 wt%). The mixture of solutions was kept stirring for 2 h. After that, AHMSNs and NH-AHMSNs that had been activated with GA were resuspended in PBS buffer (pH = 6.5) supplemented with UOx (5 mg/mL) after three washes with PBS buffer (pH = 6.5). The UOx conjugation approach was conducted overnight at room temperature with moderate shaking. Then, AHMSNs@UOx and NH-AHMSNs@UOx was obtained and washed with DI water three times.

Preparation of AHMSNs@UOx@SC and NH-AHMSNs@UOx@SC

Sodium citrate and the obtained AHMSNs@UOx and NH-AHMSNs@UOx were mixed for 12 h with moderate shaking to obtained AHMSNs@UOx@SC and NH-AHMSNs@UOx@SC. AHMSNs@UOx@SC and NH-AHMSNs@UOx@SC was collected in DI water and stored at 4 °C for future experiments.

Encapsulation efficiency and loading capacity

AHMSNs@UOx@SC sample was centrifuged at speed of 3420 g for 5 min, and the amount of UOx in the supernatant was measured using a BCA protein kit with a UV spectrophotometer at 570 nm. The following equations were employed to determine the encapsulation efficiency (EE) and the loading capacity (LC):

$$\mathrm{EE}\,(\%) = \frac{(A-B)}{A} \times 100 \tag{1}$$

$$\mathrm{LC}\,(\%) = \frac{(A-B)}{M} \times 100 \tag{2}$$

where A is the total amount of UOx, B is the amount of UOx remaining in the supernatant, M is the mass of AHMNs@UOx@SC.

SDS-PAGE measurement

The final concentration of acrylamide in the separating gel was 10%, and polyacrylamide gels were prepared in accordance with a standard protocol. The loading buffer was combined with 15 µL of each sample (40 µg of proteins) and boiled at 100 °C for 5 min before being inserted onto the electrophoresis platform. Stacking gel electrophoresis was performed in the BIO-RAD Electrophoresis System at a constant voltage of 90 V, while separating gel electrophoresis was performed at 120 V. The loading reagent is allowed to run for 12 cm of the separating gel before the electrophoresis concludes. After that, the gels were stained with Coomasie blue stain and recorded for contrast.

Nanomotor movement

The nanomotor movement was studied using a Nikon Ti2-A microscope with 40 × objective. A 0.8 mm high Petri dish was prepared with 10 µL of AHMSNs@UOx@SC and NH-AHMSNs@UOx@SC solution with the intended concentration and 10 µL of UA solution with variable concentrations. To mitigate the drifting effect, a coverslip was positioned over the dish. The concentration of UA solution was 0, 200, 400, and 600 µM, respectively.

COMSOL simulation

The fluxes near the surface were restricted to the direction vertical to the surface, and the assumption of a thin double layer was employed[52]. Conventional ion fluxes were disregarded owing to their relatively negligible contribution. An axisymmetric 2D model was built in the COMSOL Multiphysics program. As is shown in Supplementary Fig. 9, the outer diameters of the AHMSNs@UOx@SC are 362 nm, the internal diameter is 302 nm, and the hole diameter is 86 nm. The COMSOL model employed creeping flow modules and electrostatics. The outer surface of the AHMSNs@UOx@SC in the electrostatics module generated an ions flux of H^+ and HCO_3^-. In addition, it contained an extrinsic surface charge density that was correlated with the flux (flux_outside) and the diffusivities of H^+ (D_{H^+}) and HCO_3^- (D_{HCO3^-}) by the formula:

$$\rho = \varepsilon E = \varepsilon \frac{J k_B T}{2 e n_0} \left\{ \frac{1}{D_{HCO3-}} - \frac{1}{D_{H^+}} \right\} \tag{3}$$

where n_0 is the bulk ion concentration and ε is the medium electrical permittivity. Since the original pH of the solution was determined to be around 5.65 when water was saturated with CO_2, the bulk concentration of protons and bicarbonate ions can be computed to be 2.24×10^{-6} mol/L. An electro-osmotic boundary condition was set up on the internal and external surface of the creeping flow module.

$$\mathrm{v} = \frac{\zeta \varepsilon}{\mu} \mathrm{E} \tag{4}$$

where υ represents the speed at which fluid moves across the motor surface due to electro-osmosis, ζ represents the zeta potential of either the outer or interior surface, μ represents the dynamic viscosity of water, and E represents the tangential component of the electric field.

Measurement of UA Degradation

UOx could catalyze the formation of allantoin, CO_2, and H_2O_2 from UA. H_2O_2 oxidizes Fe^{2+} in potassium ferricyanide to form Fe^{3+}. Fe^{3+} further condenses with phenol and 4-aminoantipyrine to form a red quinone compound with a characteristic absorption peak at 505 nm. Hence, the catalytic degradation of UA was observed by employing a UV-Visible spectrophotometer to measure the variations in absorbance at 505 nm every 1 h. The typical reaction system contained a kind of UA (1000 µM), NH-AHMSNs@UOx@SC, and AHMSNs@UOx@SC (250 µg/mL) in a 50 mM PBS 8.0 phosphate buffer at 25 °C.

Detection of accumulated H_2O_2 after UA degradation

The accumulated H_2O_2 after UA degradation was detected using hydrogen peroxide assay kit at the aforementioned time intervals. Following UA degradation catalyzed by AHMSNs@UOx@SC, NH-AHMSNs@UOx@SC, AHMSNs@UOx, NH-AHMSNs@UOx, and UOx, the catalysts were eliminated via centrifugation at 9500 *g* for 15 min. The mixture of xylenol orange and Fe^{2+} was added to the supernatant, which was then incubated at room temperature for 30 min. The absorbance at 570 nm was subsequently measured. The H_2O_2 level was determined using standard curves based on particular protein concentrations.

Resistance against pH, high temperature, and trypsin digestion

pH Resistance: The residual catalytic activities of all samples (UOx, NH-AHMSNs@UOx@SC, and AHMSNs@UOx@SC dissolved in 50 mM PBS with varying pH) were assessed at 25 °C after incubation for 30 min.

Temperature Resistance: All samples (UOx, NH-AHMSNs@UOx@SC, and AHMSNs@UOx@SC dissolved in 50 mM pH = 8.0 PBS) were incubated at varying temperatures (40, 50, 60, 70 °C) for 30 min. Finally, all tests were conducted at a temperature of 25 °C.

Protease Resistance: At 37 °C, all samples (UOx, NH-AHMSNs@UOx@SC, and AHMSNs@UOx@SC dissolved in 50 mM pH = 8.0 PBS) were incubated with 1 mg/mL trypsin. Residual catalytic activities of the samples were estimated at 25 °C at a variety of temperatures.

Cytotoxicity assays

After seeding 10^5 cells per well into a 96-well and incubating them for 24 h, the cells were treated with 1000×10^{-6} M UA. A further 12 h of incubation were conducted with the addition of 250 µg/mL AHMSNs@UOx, NH-AHMSNs@UOx, AHMSNs@UOx@SC or NH-AHMSNs@UOx@SC. Cell viability was ultimately determined using MTT reagent, an indicator utilized to probe the viability of cells.

Reactive Oxygen Species (ROS) detection

The production of ROS was measured utilizing a ROS Assay Kit. A concentration of 1000×10^{-6} M UA was applied to 4T1 cells were cultured in a 96-well plate. After that, 250 µg/mL of AHMSNs@UOx, NH-AHMSNs@UOx, AHMSNs@UOx@SC or NH-AHMSNs@UOx@SC was added for a 12-h incubation. Then 10 µM 2′,7′- dichlorofluorescin diacetate (DCFH-DA) was added into 4T1 cells for 30 min at 37 °C. The nucleus was stained with Hoechst 33342. The cells were subsequently washed three times with PBS solution (pH 7.4) and then imaged using a inverted fluorescence microscope.

Preparation of SSF

A SSF was prepared by combining NaCl (4.0 g/L), KCl (0.1 g/L), Na_2HPO_4 (0.72 g/L), KH_2PO_4 (0.12 g/L), hyaluronic acid (1.5 g/L), and ultrapure water to a concentration of 100%[53].

Preparation of MSU Crystals

In detail, 4 g of UA was dissolved in 775 mL of water. Following the addition of 25 mL of NaOH (1 mol/L) to the UA solution, the mixture was heated to completely dissolve the UA. Following natural cooling with agitation, the pH of the UA solution was adjusted to 7.0. A 860-g filtration was performed for 2 min on the white turbid fluid. After reducing the supernatant to 4 °C overnight, the crystals underwent filtration in preparation for lyophilization. Through microscopy, recovered MSU crystals were observed after being suspended in sterile saline at a concentration of 20 mg/mL. From Supplementary Fig. 20, the MSU were shown with needle-like crystals.

Acute gouty arthritis model

For the acute gouty arthritis model, 30 rodents were randomly assigned to five groups, each of which was designated as the control group, MSU, UOx, AHMSNs@UOx, and AHMSNs@UOx@SC, respectively. Figure 4a briefly illustrated the experimental scheme. Under the anesthetic of isoflurane, acute gout models were induced by administering MSU (20 mg/mL, 100 µL) intra-articularly into the right knee joint of rats. The control group had been administered with a 100 µL injection of normal saline. Then UOx, AHMSNs@UOx, and AHMSNs@UOx@SC (50 µL) were injected into the joint cavity. Through utilizing a Vernier calliper, the distance between the medial and lateral condyles of the knees in each group of rodents was determined by observing their knee diameters. Anesthesia was utilized to extract the synovial fluid and blood collected by the cardiac punctures of rats for five groups for ELISA analysis of inflammatory factors, including TNF-α, IL-8, and IL-β.

Repeated intra-articular MSU-induced gouty arthritis model

Figure 5a briefly illustrated the experimental scheme. Then, on Days 1 and 5, rats were administered 100 µL of MSU crystals intra-articularly in the right hind knee while under anesthesia. The MSU crystal injections were repeated for 7 weeks. Rats of the control group received 100 µL of PBS injected at the same time each week. 25 rats were divided at random into five groups after inflammation observed at day 50. The treatment began at day 50 with five groups ($n = 5$). 100 µL of PBS, UOx, AHMSNs@UOx, and AHMSNs@UOx@SC were administered via intraarticular injection at the right knee joint. The joint edema of each rat was photographed and quantified under anesthesia at the conclusion of the experiment. Following that, a blood sample of 1 mL was collected from the exposed rat heats to analyze inflammatory factors, just an in the acute gout model. The rats were subsequently sacrificed under deep anesthesia. The right hind knee joints were obtained and immobilized at 4 °C for one week using 4% paraformaldehyde in preparation for micro focal computed tomography scanning (Micro-CT). Images reconstructed using three-dimensional CT were acquired to quantify the degree of joint injury. A region of the subchondral plate measuring 1.2 mm × 3.7 mm was chosen to compute the bone mineral density (BMD). As the region of interest for the subchondral trabecular bone analysis, a region of trabecular bone measuring 1.2 mm × 3.7 mm was chosen from beneath the subchondral plate. Then the bone volume/total volume, BV/TV; trabecular number (plate model), Tb.N (pl); and trabecular separation (plate model), Tb. Sp (pl) were calculated. The histopathological examination of the right hind knee joint of the rat was conducted using safranin-O/fast green staining and H&E staining.

H_2O_2 quantification within the Joint Cavity of Recurrent Gouty Rats

A Hydrogen Peroxide assay kit (A064-1-1, Nanjing Jiancheng Bioengineering Institute) was utilized to quantify the H_2O_2 concentration in the joint cavity of the rats, wherein H_2O_2 interacted with molybdic acid to generate a complex exhibiting maximum absorbance at 405 nm. For the detection of H_2O_2 accumulation in the joint cavity, fresh joints were collected and homogenized in ice-cold saline to obtain 10% homogenates. The homogenate was then centrifuged at 13680 g for 10 min, and the supernatant was utilized to ascertain the protein concentration (A405-3, Nanjing Jiancheng Bioengineering Institute). Subsequently, the accumulation of H_2O_2 in the joint cavity of the rats was detected by employing a UV-Vis spectrophotometer in absorbance at 405 nm.

Elimination dynamics of AHMSNs@UOx@SC

Cy7-NHS was loaded into AHMSNs@UOx@SC via impregnation to prepare Cy7 labled AHMSNs@UOx@SC. Then, Cy7 labled AHMSNs@UOx@SC were injected into the joint cavity of gouty rats. The rats were anesthetized with isoflurane for 3 min, and fluorescence images were captured at various intervals with AniView Kirin in vivo imaging system. A microdialysis (MD) system was employed to analyze the elimination dynamics of AHMSNs@UOx@SC in gouty rats. The microdialysis probe was implanted into the joint via surgery under anesthesia. The samples were stabilized and equilibrated with normal saline at a rate of 2 µL/min for 1 h. Following the injection of AHMSNs@UOx@SC, the reflux fluid was collected at specified intervals. A 0.5-mL blood samples was obtained simultaneously. Concentrations of the silicon in the reflux fluid and blood were assessed utilizing ICP-MS.

Statistical analysis

Data analysis was conducted using the software Microsoft Office Excel 2019, Origin 9, GraphPad Prism 8.3, and Image J (1.52a). Flow cytometry were analyzed on Flowjo_V10 software. Living image software (kirin) was used to analyse fluorescent images. The secondary stucture of uricase was computed by CONTIN method using CDPro software. The results were presented as the mean value with standard deviation (SD). Statistical analysis was performed by the student t-test (two-tailed). $P < 0.05$ was deemed indicative of a statistically significant distinction between the two groups.

Reporting summary

Further information on research design is available in the Nature Portfolio Reporting Summary linked to this article.

Data availability

The source data generated in this study are provided in the Supplementary Information/Source Data file. The full image dataset is available from the corresponding author upon request. Source data are provided with this paper. Source data is available for Figs. 2–6 and Supplementary Figs. 1–8, 10, 11, 13, 14, 17, 18, 21–23 and 25 in the associated source data file. Figshare. Dataset. https://doi.org/10.6084/m9.figshare.28040396. Source data are provided with this paper.

References

1. Dalbeth, N. et al. Gout. *Nat. Rev. Dis. Primers* **5**, 69 (2019).
2. Neilson, J., Bonnon, A., Dickson, A. & Roddy, E. Gout: diagnosis and management-summary of NICE guidance. *BMJ* **378**, o1754 (2022).
3. Saul, H., Deeney, B., Swaithes, L. & Roddy, E. How common are side effects of treatment to prevent gout flares when starting allopurinol? *BMJ* **384**, q514 (2024).
4. Stamp, L. et al. Is colchicine prophylaxis required with start-low go-slow allopurinol dose escalation in gout? A non-inferiority randomised double-blind placebo-controlled trial. *Ann. Rheum. Dis.* **82**, 1626–1634 (2023).
5. Fraisse, L. et al. A colorimetric 96-well microtiter plate assay for the determination of urate oxidase activity and its kinetic parameters. *Anal. Biochem.* **309**, 173–179 (2002)..
6. Schlesinger, N., Pérez-Ruiz, F. & Lioté, F. Mechanisms and rationale for uricase use in patients with gout. *Nat. Rev. Rheumatol.* **19**, 640–649 (2023).
7. Dong, Y. et al. Nano-sized platinum as a mimic of uricase catalyzing the oxidative degradation of uric acid. *Phys. Chem. Chem. Phys.* **13**, 6319–6324 (2011).
8. Sheldon, R. A. & van Pelt, S. Enzyme immobilisation in biocatalysis: why, what and how. *Chem. Soc. Rev.* **42**, 6223–6235 (2013).
9. Liu, Y. et al. Biomimetic enzyme nanocomplexes and their use as antidotes and preventive measures for alcohol intoxication. *Nat. Nanotechnol.* **8**, 187–192 (2013).
10. Gao, W., Pei, A., Feng, X., Hennessy, C. & Wang, J. Organized Self-Assembly of Janus Micromotors with Hydrophobic Hemispheres. *J. Am. Chem. Soc.* **135**, 998–1001 (2013).
11. Liu, L. et al. Magnetically actuated biohybrid microswimmers for precise photothermal muscle contraction. *ACS Nano* **16**, 6515–6526 (2022).
12. Zhou, F., Shu, W., Welland, M. E. & Huck, W. T. S. Highly reversible and multi-stage cantilever actuation driven by polyelectrolyte brushes. *J. Am. Chem. Soc.* **128**, 5326–5327 (2006).
13. Li, H. et al. Medical micro- and nanomotors in the body. *Acta Pharm. Sin. B* **13**, 517–541 (2023).
14. Wan, M., Li, T., Chen, H., Mao, C. & Shen, J. Biosafety, Functionalities, and Applications of Biomedical Micro/nanomotors. *Angew. Chem. Int. Ed.* **60**, 13158–13176 (2021).
15. Esteban-Fernández de Ávila, B. et al. Multicompartment tubular micromotors toward enhanced localized active delivery. *Adv. Mater.* **32**, 2000091 (2020).
16. Díez, P. et al. Ultrafast directional Janus Pt–mesoporous silica nanomotors for smart drug delivery. *ACS Nano* **15**, 4467–4480 (2021).
17. Wu, Y. et al. Gastric acid powered nanomotors release antibiotics for in vivo treatment of Helicobacter pylori infection. *Small* **17**, 2006877 (2021).
18. Yuan, K., de la Asunción-Nadal, V., Jurado-Sánchez, B. & Escarpa, A. 2D nanomaterials wrapped Janus micromotors with built-in multiengines for bubble, magnetic, and light driven propulsion. *Chem. Mater.* **32**, 1983–1992 (2020).
19. Draz, M. S. et al. DNA engineered micromotors powered by metal nanoparticles for motion based cellphone diagnostics. *Nat. Commun.* **9**, 4282 (2018).
20. Liang, Z. & Fan, D. Visible light–gated reconfigurable rotary actuation of electric nanomotors. *Sci. Adv.* **4**, eaau0981 (2018).
21. Shao, L. & Käll, M. Light-driven rotation of plasmonic nanomotors. *Adv. Funct. Mater.* **28**, 1706272 (2018).
22. Hansen-Bruhn, M. et al. Active intracellular delivery of a Cas9/sgRNA complex using ultrasound-propelled nanomotors. *Angew. Chem. Int. Ed.* **57**, 2657–2661 (2018).
23. Ilic, O. et al. Topologically enabled optical nanomotors. *Sci. Adv.* **3**, e1602738 (2017).
24. Wan, M. et al. Platelet-derived porous nanomotor for thrombus therapy. *Sci. Adv.* **6**, eaaz9014 (2020).
25. Mou, F. et al. ZnO-based micromotors fueled by CO_2: the first example of self-reorientation-induced biomimetic chemotaxis. *Natl. Sci. Rev.* **8**, nwab066 (2021).
26. Xiong, K., Xu, L., Lin, J., Mou, F. & Guan, J. Mg-based micromotors with motion responsive to dual stimuli. *Research* **2020**, 6213981 (2020).
27. Hortelão, A. C., Carrascosa, R., Murillo-Cremaes, N., Patiño, T. & Sánchez, S. Targeting 3D bladder cancer spheroids with urease-powered nanomotors. *ACS Nano* **13**, 429–439 (2019).
28. Feng, Y. et al. Self-adaptive enzyme-powered micromotors with switchable propulsion mechanism and motion directionality. *Appl. Phys. Rev.* **8**, 011406 (2021).
29. Hortelão, A. C. et al. LipoBots: Using liposomal vesicles as protective shell of urease-based nanomotors. *Adv. Funct. Mater.* **30**, 2002767 (2020).
30. Wang, L. et al. Enzyme conformation influences the performance of lipase-powered nanomotors. *Angew. Chem. Int. Ed.* **59**, 21080–21087 (2020).
31. Yang, Z. et al. Ultrasmall Enzyme-powered Janus nanomotor working in blood circulation system. *ACS Nano* **17**, 6023–6035 (2023).
32. Mathesh, M., Bhattarai, E. & Yang, W. 2D active nanobots based on soft nanoarchitectonics powered by an ultralow fuel concentration. *Angew. Chem. Int. Ed.* **61**, e202113801 (2022).

33. Kankala, R. K. et al. Nanoarchitectured structure and surface biofunctionality of mesoporous silica nanoparticles. *Adv. Mater.* **32**, 1907035 (2020).
34. Xu, D. et al. Enzymatic micromotors as a mobile photosensitizer platform for highly efficient on-chip targeted antibacteria photodynamic therapy. *Adv. Funct. Mater.* **29**, 1807727 (2019).
35. Keller, S., Teora, S. P., Hu, G. X., Nijemeisland, M. & Wilson, D. A. High-throughput design of biocompatible enzyme-based hydrogel microparticles with autonomous movement. *Angew. Chem. Int. Ed.* **57**, 9814–9817 (2018).
36. Patiño, T. et al. Influence of enzyme quantity and distribution on the self-propulsion of non-Janus Urease-powered micromotors. *J. Am. Chem. Soc.* **140**, 7896–7903 (2018).
37. Ma, X., Wang, X., Hahn, K. & Sánchez, S. Motion control of urea-powered biocompatible hollow microcapsules. *ACS Nano* **10**, 3597–3605 (2016).
38. Zhang, X., Guan, R.-F., Wu, D.-Q. & Chan, K.-Y. Enzyme immobilization on amino-functionalized mesostructured cellular foam surfaces, characterization and catalytic properties. *J. Mol. Catal. B: Enzym.* **33**, 43–50 (2005).
39. Zhuang, X.-D. et al. Conjugated-polymer-functionalized graphene oxide: synthesis and nonvolatile rewritable memory effect. *Adv. Mater.* **22**, 1731–1735 (2010).
40. Patiño, T., Arqué, X., Mestre, R., Palacios, L. & Sánchez, S. Fundamental aspects of enzyme-powered micro- and nanoswimmers. *Acc. Chem. Res.* **51**, 2662–2671 (2018).
41. Ma, X. et al. Enzyme-powered hollow mesoporous Janus nanomotors. *Nano Lett.* **15**, 7043–7050 (2015).
42. Sun, H. L. et al. Function of uric acid transporters and their inhibitors in hyperuricaemia. *Front. Pharmacol.* **12**, 667753 (2021).
43. Chen, D. et al. Low-potential detection of endogenous and physiological uric acid at uricase–thionine–single-walled carbon nanotube modified electrodes. *Anal. Chem.* **82**, 2448–2455 (2010).
44. Lin, Y.-Y. et al. Etoricoxib prevents progression of osteolysis in repeated intra-articular monosodium urate-induced gouty arthritis in rats. *J. Adv. Res.* **24**, 109–120 (2020).
45. Bandyopadhyay, U., Das, D. & Banerjee, R. K. Reactive oxygen species: oxidative damage and pathogenesis. *Curr. Sci.* **77**, 658–666 (1999).
46. Rühle, B., Saint-Cricq, P. & Zink, J. I. Externally controlled nanomachines on mesoporous silica nanoparticles for biomedical applications. *ChemPhysChem* **17**, 1769–1779 (2016).
47. Busso, N. & So, A. Gout. Mechanisms of inflammation in gout. *Arthritis Res. Ther.* **12**, 206 (2010).
48. Qi, G. et al. Facile and scalable synthesis of monodispersed spherical capsules with a mesoporous shell. *Chem. Mater.* **22**, 2693–2695 (2010).
49. Zhao, C. et al. Structural transformative antioxidants for dual-responsive anti-inflammatory delivery and photoacoustic inflammation imaging. *Angew. Chem. Int. Ed.* **60**, 14458–14466 (2021).
50. Fournier, R. O. & Rowe, J. J. The solubility of amorphous silica in water at high temperatures and high pressures. *Am. Mineral.* **62**, 1052–1056 (1977).
51. Bindini, E. et al. Following in situ the degradation of mesoporous silica in biorelevant conditions: at last, a good comprehension of the structure influence. *ACS Appl. Mater. Interfaces* **12**, 13598–13612 (2020).
52. Liu, C., Zhou, C., Wang, W. & Zhang, H. P. Bimetallic microswimmers speed up in confining channels. *Phys. Rev. Lett.* **117**, 198001 (2016).
53. Marques, M. R. C., Loebenberg, R. & Almukainzi, M. J. D. T. Simulated biological fluids with possible application in dissolution testing. *Dissolut. Technol.* **18**, 15–28 (2011).

Acknowledgements

This work was supported by National Key Research and Development Program of China (2022YFA1206900, Y.T.), National Natural Science Foundation of China (22175083, Y.T.; 22375224, F.P.; 22405119, L.L.), China Postdoctoral Science Foundation (2023M741595, L.L.), and Postdoctoral Fellowship Program of China Postdoctoral Science Foundation (GZB20230292, L.L.).

Author contributions

L.L. and Y.T. proposed and designed the whole process of the study. L.L., X.L., Y.C., J.G., Y.J., and Y.Y. performed the experiments and analyzed the data. L.L. and Y.T. wrote the manuscript. Y.T., F.P., and P.W. supervised the project.

Competing interests

The authors declare no competing interests.

Additional information

Supplementary information The online version contains supplementary material available at https://doi.org/10.1038/s41467-025-56100-9.

Correspondence and requests for materials should be addressed to Peng Wang, Fei Peng or Yingfeng Tu.

Peer review information *Nature Communications* thanks Motilal Mathesh and the other, anonymous, reviewers for their contribution to the peer review of this work. A peer review file is available.